Composite Structures 374 (2025) 119711

Contents lists available at ScienceDirect

Composite Structures

journal homepage: www.elsevier.com/locate/compstruct

NATM tunnel as multiscale composite structure: The essential role of shell-to-ground shear transfer☆

Raphael Scharf, Christian Hellmich *

Institute for Mechanics of Materials and Structures, TU Wien (Vienna University of Technology), Karlsplatz 13/202, 1040 Vienna, Austria

ARTICLE INFO

Keywords:
New Austrian Tunneling Method
Composite structure
Nonlinear aging viscoelasticity
Shear transfer
Analytical mechanics
Principle of virtual power
Shell theory

ABSTRACT

The New Austrian Tunneling Method (NATM) realizes an integrated ground–shell composite structure, namely a displacement-monitored shotcrete shell surrounded by rock bolt-reinforced ground. The present paper focusses on the shear transfer between ground and shell, as experimentally evidenced by direct shear tests of soil or rock samples moved over concrete surfaces. A multiscale analytical structural mechanics approach allows for translation of geodetical measurements into external and internal shell forces and stresses. Key ingredients of the approach are the continuum mechanics-related format of the Principle of Virtual Power, thin shell kinematics, i.e. virtual motions of rigid generator lines remaining orthogonal to the shell midsurface, and aging nonlinear viscoelasticity modeling of shotcrete. Application of the new method to Sieberg tunnel, an NATM benchmark example, shows that consideration of ground shear reduced the utilization degree of the shell by some 50%: Shell-to-ground shear transfer turns out as an essential feature of NATM tunneling.

1. Introduction

Different from its historical predecessors where the tunnel shells have been regarded as means to "carry" loads imposed by the rock or ground surrounding the tunnel opening, the New Austrian Tunneling Method (NATM), established by Rabcewicz in the 1960s [1–3], comprises measures to integrate the tunnel shell into the surrounding ground, so as to realize a joint load carrying system which encompasses both the tunnel shell and the surrounding rock or ground. These measures are [4]: (i) a flexible shell made of sprayed concrete ("shotcrete") reinforced by steel meshes, (ii) rock bolts connecting the shell with the surrounding ground, and (iii) dedicated deformation monitoring for revealing the actual load carrying behavior and the safety level of the tunnel shell.

In this sense, an NATM shell may be regarded as epitome for a "composite structure" when seeing this term as an analogue to the term "composite material": two distinct components (shell and ground) make up the overall structure, and they are both essential for the functioning of the latter. Accordingly, the force transfer between tunnel shell and ground has been of central interest ever since the NATM has been established. In this context, so-called confinement–convergence diagrams [5,6] or characteristic interaction curves [7,8] have remained the customary standard: A characteristic change of the radius of the cross-sectional opening of the tunnel is related to a scalar pressure-type quantity representing the mechanical ground–shell interaction, together with categorizations such as "constraining pressure" or "loosening pressure" [9]. Approaches beyond this 1D perception include evaluations of geodetic displacement monitoring data in the context of so-called "hybrid methods" [10–13]. These methods reconstruct displacement fields from data recorded at distinct measurement points, and relate the latter, through compatibility conditions and constitutive modeling of early-age concrete, to stress fields inside the tunnel shell; and, via equilibrium conditions, to traction force fields at the shell–ground interface [14]. As a corresponding result for the Sieberg tunnel [15], a part of the high capacity railway line from Vienna to Salzburg in Austria, quadratic interpolation of geodetic displacement data along the tunnel circumference, in terms of circumferential, radial, and longitudinal components, yielded ground pressures dominating at the upper portion of the tunnel shell, and significant shear traction forces acting, in upwards direction, on the lateral portions of the shell [14]. Somewhat different ground loading characteristics are obtained for the very same tunnel and cross section, if polynomial spatial distributions are not prescribed for the displacements, but for the physical primitives driving these displacements, namely for the normal traction forces [16,17]. The latter enter cylindrical shell theory as external forces, together with impost forces acting at the ends of the top heading. Such a modeling approach results in quasi-uniform ground pressure distributions along the shell circumference [16,17].

☆ This article is part of a Special issue entitled: 'Advanced materials models' published in Composite Structures.

* Corresponding author.
E-mail address: christian.hellmich@tuwien.ac.at (C. Hellmich).

https://doi.org/10.1016/j.compstruct.2025.119711
Received 1 July 2025; Received in revised form 24 September 2025; Accepted 27 September 2025
Available online 3 October 2025

Table 1
Direct shear test results for soil-concrete interfaces.

Reference	Soil type	Normal stress range [MPa]	Range of shear-over-normal stress ratio [–]
Zong-Ze et al. (1995) [19]	sand	0.30	0.67
Hossain et al. (2014) [20]	decomposed granite	0.05 … 0.30	0.55 … 1.20
Chen et al. (2015) [21]	clay	0.10 … 0.60	0.38 … 1.29
Yavari et al. (2016) [22]	clay	0.01 … 0.10	0.30 … 0.50
Ilori et al. (2017) [23]	cohesion less soil	0.14 … 0.43	0.14 … 1.52
Haeri et al. (2019) [24]	clay silt	0.08 … 0.50	0.47 … 1.56
Xiao et al. (2019) [25]	sandy silty clay	0.03 … 0.10	0.20 … 1.08
Yazdani et al. (2019) [26]	clay	0.15 … 0.30	0.27 … 0.42
Maghsoodi et al. (2020) [27]	sand, clay	0.10 … 0.30	0.26 … 1.12
Janipour et al. (2022) [28]	sand	0.05 … 0.20	0.25 … 0.85
Hashemi et al. (2022) [29]	clay	0.05 … 0.40	0.20 … 0.52
Liu et al. (2023) [30]	sand	0.10 … 0.30	0.40 … 0.64
Li et al. (2024) [31]	gravelly sand	0.05 … 0.25	0.62 … 0.98

Notably, these two different approaches were characterized by an *ad hoc* consideration of shear traction forces (through either obtaining them as a "post-processing" result stemming from a particular choice of displacement interpolation functions, or through setting them, in an *a priori* fashion, to zero). Aiming at an improvement of this situation, the present contribution focuses on a dedicated, and more physical treatment of shear traction forces and their role in NATM tunnel engineering. More precisely, according to Coulomb's friction law, the present investigation concerns different ratios between normal and shear traction forces acting on an NATM tunnel shell. Building thereby on results reported in the PhD thesis of Scharf [18], we once again resort to the benchmark example of the Sieberg tunnel.

Accordingly, the remainder of the current paper is organized as follows: After reviewing experimental results concerning the traction force transfer at the shell–ground interface, see Section 2, the equilibrium of such forces with the internal forces transgressing the tunnel shell is mathematically derived from the Principle of Virtual Power, in Section 3. Corresponding differential equations are first analytically solved (as described in Section 4) and then combined with viscoelastic material modeling (as described in Section 5). This allows for displacement-to-force conversion (as described in Section 6). Results are discussed in Section 7, before the paper is concluded in Section 8.

2. Ground–shell traction transfer: review of experimental evidence

Fictitious Euler cutting [32,33] of the shell from the surrounding ground yields traction force fields acting on the tunnel shell, together with oppositely directed traction force fields acting on the ground, according to the so-called action–reaction principle, also called traction force equilibrium at boundaries of subsystems [34]. With plain strain conditions [16] implying the longitudinal traction transfer to vanish, the ground–shell interaction is fully governed by normal and circumferential shear components, with the ratio of their magnitudes depending on the nature of the shell-to-ground interface. This dependence is amply documented in the open literature, as the result of so-called direct shear tests. These tests are characterized as follows [35]: A soil sample is placed on the surface of a building material, such as concrete. It is subjected to vertical compression by a force applied through a top cap. Simultaneously, the sample is laterally confined by the walls of a shear box, which moves it horizontally across the underlying material surface. The observed ratios of shear to normal traction components, reminiscent of a "friction coefficient", may vary quite extensively, depending on the type of soil tested, see Table 1 for a compilation of corresponding test results. The benchmark example dealt with in Section 4, Section 6, and Section 7 concerns measurement cross section MC1452 of the Sieberg tunnel, a railway tunnel driven in clayey marl [15]. This suggests to study the effect of shear-of-normal stress ratios of 0.25, 0.50, 0.75, and 1.00; together with the classical limit case of normal stress (called ground pressure) only.

3. Equilibrium of thin cylindrical tunnel shells loaded by normal and shear traction forces arising from ground action

The Principle of Virtual Power (PVP) as given by Germain [36–39], standing in line with a wealth of earlier formulations since the dawn of mechanics as a scholarly discipline [40], is a general statement on the movement (including quasi-static equilibrium) of a mechanical system. More precisely, the virtual powers are linear forms [41] on the internal and external force quantities, with arbitrary arguments called virtual velocities; and quasi-static equilibrium is ensured through the sum of the virtual powers of the external and internal forces being zero. The present contribution considers a continuous system where significant variation of forces is restricted to the cross section through a tunnel shell, while force variations are quasi-negligible along the driving direction of the tunnel. Accordingly, power densities per unit length of tunnel driving direction are employed herein, with the virtual power density of external forces, denoted by $\mathcal{P}^{\text{ext}}$, then taking the following mathematical form:

$$\mathcal{P}^{\text{ext}}\left[\hat{\mathbf{v}}(\mathbf{x})\right] = \int_C \mathbf{T}(\mathbf{x},\mathbf{n})\cdot\hat{\mathbf{v}}(\mathbf{x})\,\mathrm{d}s + \int_A \mathbf{f}(\mathbf{x})\cdot\hat{\mathbf{v}}(\mathbf{x})\,\mathrm{d}A\,, \quad \forall\hat{\mathbf{v}}\in\mathbb{R}^3 \text{ with } \frac{\partial\hat{\mathbf{v}}}{\partial\mathbf{x}}\in\mathbb{R}^3\otimes\mathbb{R}^3\,. \tag{1}$$

In Eq. (1), $\hat{\mathbf{v}}$ stands for the virtual velocity, i.e. for an arbitrary differentiable real vector field, $\mathbf{x}$ denotes the position vector labeling points within the cross-sectional area A and its contour (boundary) C, $\mathbf{f}$ denotes the volume force density, $\mathbf{T}$ denotes the surface force density or traction vector acting on a contour element $\mathrm{d}s$ with unit normal $\mathbf{n}$. On the other hand, the power density of the internal forces, denoted as $\mathcal{P}^{\text{int}}$, reads, for the current application, as

$$\mathcal{P}^{\text{int}}\left[\hat{\mathbf{v}}(\mathbf{x})\right] = -\int_A \boldsymbol{\sigma}(\mathbf{x}) : \hat{\mathbf{d}}(\mathbf{x})\,\mathrm{d}A\,, \quad \forall\hat{\mathbf{v}}\in\mathbb{R}^3 \text{ with } \frac{\partial\hat{\mathbf{v}}}{\partial\mathbf{x}}\in\mathbb{R}^3\otimes\mathbb{R}^3\,. \tag{2}$$

In Eq. (2), $\boldsymbol{\sigma}$ denotes the symmetric second-order Cauchy stress tensor, and

$$\hat{\mathbf{d}}(\mathbf{x}) = \nabla^S\hat{\mathbf{v}}(\mathbf{x}) = \frac{1}{2}\left[\frac{\partial\hat{\mathbf{v}}}{\partial\mathbf{x}} + \left(\frac{\partial\hat{\mathbf{v}}}{\partial\mathbf{x}}\right)^T\right], \tag{3}$$

stands for the virtual Eulerian strain rate tensor. The mathematical form of the Principle of Virtual Power hence takes the mathematical form

$$\mathcal{P}^{\text{ext}}\left[\hat{\mathbf{v}}(\mathbf{x})\right] + \mathcal{P}^{\text{int}}\left[\hat{\mathbf{v}}(\mathbf{x})\right] = 0\,, \quad \forall\hat{\mathbf{v}}\in\mathbb{R}^3 \text{ with } \frac{\partial\hat{\mathbf{v}}}{\partial\mathbf{x}}\in\mathbb{R}^3\otimes\mathbb{R}^3\,, \tag{4}$$

with the power densities of the external and the internal forces, respectively, obeying Eqs. (1) and (2).

According to the theory of thin shells developed in the framework of the principle of virtual power [42,43], the equilibrium is governed by the virtual motion of straight and rigid generator lines with length

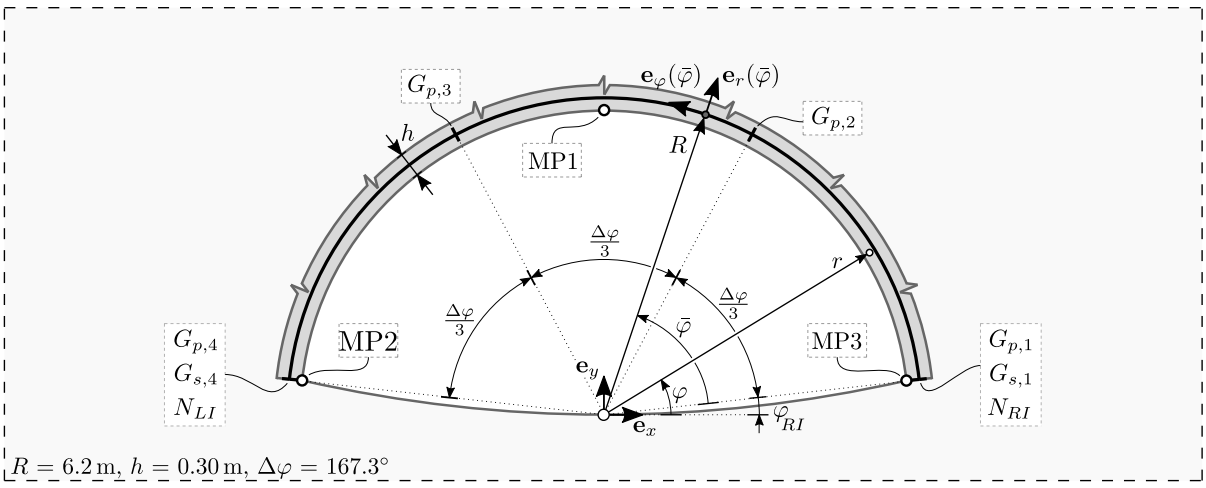

Fig. 1. Geometrical and mechanical characteristics of structural model of measurement cross section MC1452 of Sieberg tunnel: Circular top heading of tunnel shell with radius R, thickness h, and opening angle $\Delta\varphi$, origin of coordinate systems in circle center, Cartesian base frame $\mathbf{e}_x$-$\mathbf{e}_y$, location-dependent polar base frame $\mathbf{e}_r(\bar\varphi)$-$\mathbf{e}_\varphi(\bar\varphi)$, classical and inclined azimuthal coordinates φ and $\bar\varphi$, radial coordinate r, circumferential positions of measurement points MPi, with $i = 1,2,3$, of unknown ground pressure intensities $G_{p,i}$, with $i = 1,\dots,4$, of shear traction force intensities $G_{s,i}$, with $i = 1,4$, and of impost forces N_i, with $i = RI, LI$.

h, being the thickness of the shell. During such virtual motions, the generator lines maintain oriented orthogonally to the shell's midsurface. Mathematically speaking, the corresponding virtual velocity field reads as [16,43]

$$\begin{aligned}\hat{\mathbf{v}}(r,\varphi) &= \mathbf{e}_r\,\hat v_r^M(\varphi) + \mathbf{e}_\varphi\left[\hat v_\varphi^M(\varphi)\frac{r}{R} - \frac{\mathrm{d}\hat v_r^M(\varphi)}{\mathrm{d}\varphi}\frac{r-R}{R}\right],\\ &\forall \hat v_\varphi^M, \hat v_r^M \in \mathbb{R} \text{ with } \frac{\mathrm{d}\hat v_r^M(\varphi)}{\mathrm{d}\varphi}, \frac{\mathrm{d}\hat v_\varphi^M(\varphi)}{\mathrm{d}\varphi} \in \mathbb{R},\\ &\text{with } R - \frac{h}{2} \le r \le R + \frac{h}{2} \text{ and } \varphi_{RI} \le \varphi \le \varphi_{LI}\,. \end{aligned} \tag{5}$$

In Eq. (5), r and φ denote the radial and azimuthal coordinates of a cylindrical coordinate system associated with a base frame $\mathbf{e}_r(\varphi)$, $\mathbf{e}_\varphi(\varphi)$, see Fig. 1; while $\hat v_r^M$ and $\hat v_\varphi^M$ stand for the radial and circumferential component of the virtual velocity field in the shell midsurface with radius R, this field spanning counterclockwisely from the right impost with coordinate φ_{RI} to the left impost with coordinate φ_{LI}.

Moreover, the present shell theory application entails further specifications of the external forces: Traction forces with components in radial and circumferential direction act at surfaces with normals $\mathbf{e}_r(\varphi)$, and traction forces with circumferential components only act at the imposts, namely on surfaces with normals oriented towards $-\mathbf{e}_\varphi(\varphi_{RI})$ and $\mathbf{e}_\varphi(\varphi_{LI})$. Furthermore, the external forces due to dead load are typically negligible with respect to the traction forces stemming from the surrounding ground and neighboring shell segments, i.e. $|\mathbf{T}| \gg h\,|\mathbf{f}|$. When considering these specifications, together with the shell-specific virtual velocities according to Eq. (5), in Eq. (1), the expression for the power density of the external forces becomes

$$\begin{aligned}&\mathcal{P}^{\mathrm{ext}}\left[\hat v_r^M(\varphi), \hat v_\varphi^M(\varphi)\right] =\\ &\quad\int_{\varphi_{RI}}^{\varphi_{LI}} T_r\big(R_{out},\varphi;\mathbf{e}_r(\varphi)\big)\times\hat v_r^M(\varphi)\times R_{out}\,\mathrm{d}\varphi\\ &+\int_{\varphi_{RI}}^{\varphi_{LI}} T_\varphi\big(R_{out},\varphi;\mathbf{e}_r(\varphi)\big)\times\hat v_\varphi^M(\varphi)\times\frac{R_{out}^2}{R}\,\mathrm{d}\varphi\\ &-\int_{\varphi_{RI}}^{\varphi_{LI}} T_\varphi\big(R_{out},\varphi;\mathbf{e}_r(\varphi)\big)\times\frac{1}{R}\frac{\mathrm{d}\hat v_r^M(\varphi)}{\mathrm{d}\varphi}\frac{h}{2}R_{out}\,\mathrm{d}\varphi\\ &+\int_{R_{in}}^{R_{out}} T_\varphi\big(r,\varphi;\pm\mathbf{e}_\varphi(\varphi)\big)\times\hat v_\varphi^M(\varphi)\,\mathrm{d}r\Big|_{\varphi_{RI}}^{\varphi_{LI}}\\ &+\int_{R_{in}}^{R_{out}} T_\varphi\big(r,\varphi;\pm\mathbf{e}_\varphi(\varphi)\big)\times\frac{\mathrm{d}\hat v_r^M(\varphi)}{\mathrm{d}\varphi}\frac{r-R}{R}\,\mathrm{d}r\Big|_{\varphi_{RI}}^{\varphi_{LI}},\\ &\forall\ \hat v_\varphi^M, \hat v_r^M \in \mathbb{R} \text{ with } \frac{\mathrm{d}\hat v_r^M(\varphi)}{\mathrm{d}\varphi}, \frac{\mathrm{d}\hat v_\varphi^M(\varphi)}{\mathrm{d}\varphi} \in \mathbb{R}, \end{aligned} \tag{6}$$

with $R_{in} = R - h/2$ and $R_{out} = R + h/2$ referring to the inner and outer radius of the tunnel shell. When considering the thin shell characteristic $h \ll R$ and introducing the notions of ground pressure G_p and ground shear traction force G_s according to

$$G_p(\varphi) = -T_r\big(R_{out},\varphi;\mathbf{e}_r(\varphi)\big)\,, \tag{7}$$

$$G_s(\varphi) = T_\varphi\big(R_{out},\varphi;\mathbf{e}_r(\varphi)\big)\,, \tag{8}$$

then the expression for the virtual power of external forces according to Eq. (6) can be simplified to

$$\begin{aligned}&\mathcal{P}^{\mathrm{ext}}\left[\hat v_r^M(\varphi), \hat v_\varphi^M(\varphi)\right] =\\ &\quad\int_{\varphi_{RI}}^{\varphi_{LI}} -G_p(\varphi)\times\hat v_r^M(\varphi)\times R\,\mathrm{d}\varphi\\ &+\int_{\varphi_{RI}}^{\varphi_{LI}} G_s(\varphi)\times\left[\hat v_\varphi^M(\varphi)\ R - \frac{\mathrm{d}\hat v_r^M(\varphi)}{\mathrm{d}\varphi}\frac{h}{2}\right]\mathrm{d}\varphi\\ &+N_{RI}(\varphi)\times\hat v_\varphi^M(\varphi_{RI}) - N_{LI}(\varphi)\times\hat v_\varphi^M(\varphi_{LI}),\\ &\forall\ \hat v_\varphi^M, \hat v_r^M \in \mathbb{R} \text{ with } \frac{\mathrm{d}\hat v_r^M(\varphi)}{\mathrm{d}\varphi}, \frac{\mathrm{d}\hat v_\varphi^M(\varphi)}{\mathrm{d}\varphi} \in \mathbb{R}, \end{aligned} \tag{9}$$

whereby right and left (compressive) impost forces were introduced according to

$$N_{RI} = \int_{R_{in}}^{R_{out}} T_\varphi\big(r,\varphi_{RI};-\mathbf{e}_\varphi(\varphi_{RI})\big)\,\mathrm{d}r\,, \tag{10}$$

$$N_{LI} = -\int_{R_{in}}^{R_{out}} T_\varphi\big(r,\varphi_{LI};\mathbf{e}_\varphi(\varphi_{LI})\big)\,\mathrm{d}r\,, \tag{11}$$

and where vanishing external impost moments were considered, i.e.

$$\begin{aligned}M_{RI} &= \int_{R_{in}}^{R_{out}} T_\varphi\big(r,\varphi_{RI};-\mathbf{e}_\varphi(\varphi_{RI})\big)\times(r-R)\,\mathrm{d}r\\ &= 0\,,\end{aligned} \tag{12}$$

$$\begin{aligned}M_{LI} &= -\int_{R_{in}}^{R_{out}} T_\varphi\big(r,\varphi_{LI};\mathbf{e}_\varphi(\varphi_{LI})\big)\times(r-R)\,\mathrm{d}r\\ &= 0\,.\end{aligned} \tag{13}$$

In this context, the shear-to-normal stress ratios of Section 2 can be re-cast in a shear activation or friction coefficient reading as

$$k_{s,p} = \frac{G_s}{G_p}\,. \tag{14}$$

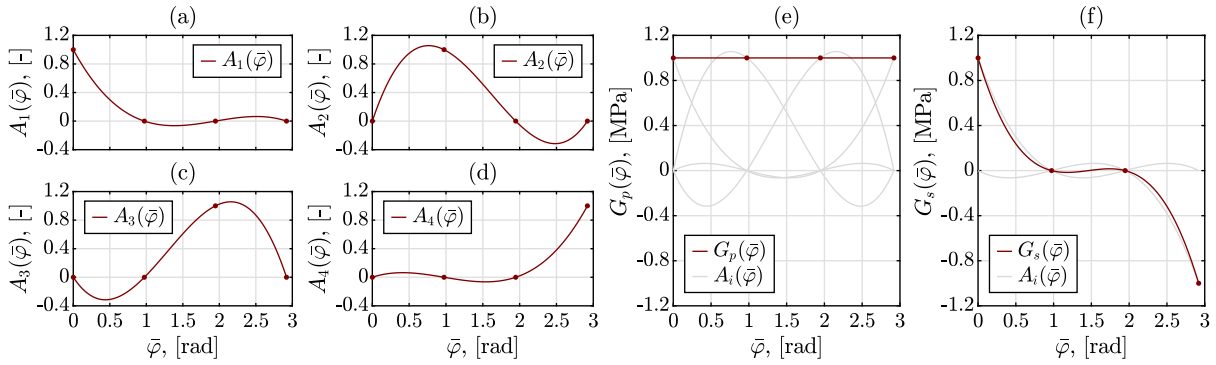

Fig. 2. Illustration of the cubic shape functions A_i, with $i = 1, 2, 3, 4$, and of the ground pressure and shear traction forces according to Eqs. (27) and (29), with $G_{p,1} = G_{p,2} = G_{p,3} = G_{p,4} = 1\,\text{MPa}$ and with $G_{s,1} = -G_{s,4} = 1\,\text{MPa}$.

Specification of the power of internal forces according to Eq. (2), for the virtual velocity field according to Eq. (5) yields

$$\begin{aligned}\mathcal{P}^{\text{int}}\left[\hat{v}_r^M(\varphi), \hat{v}_\varphi^M(\varphi)\right] = \\ -\int_{\varphi_{RI}}^{\varphi_{LI}} \int_{R_{in}}^{R_{out}} \sigma_{\varphi\varphi}(r,\varphi) \left\{ \frac{\hat{v}_r^M(\varphi)}{r} + \frac{1}{r}\frac{\mathrm{d}\hat{v}_\varphi^M(\varphi)}{\mathrm{d}\varphi} \right. \\ \left. -\frac{r-R}{rR}\left[\frac{\mathrm{d}^2\hat{v}_r^M(\varphi)}{\mathrm{d}\varphi^2} - \frac{\mathrm{d}\hat{v}_\varphi^M(\varphi)}{\mathrm{d}\varphi}\right] \right\} r\,\mathrm{d}r\,\mathrm{d}\varphi\,, \\ \forall\ \hat{v}_\varphi^M, \hat{v}_r^M \in \mathbb{R} \text{ with } \frac{\mathrm{d}\hat{v}_r^M(\varphi)}{\mathrm{d}\varphi}, \frac{\mathrm{d}\hat{v}_\varphi^M(\varphi)}{\mathrm{d}\varphi} \in \mathbb{R}\,.\end{aligned} \tag{15}$$

whereby $\sigma_{\varphi\varphi}$ denotes the normal stress component associated with direction $\mathbf{e}_\varphi(\varphi)$. As the midsurface-related virtual velocities do not depend on the radial component r, they can be taken out of the corresponding integrals. This yields an alternative form of the virtual power of internal forces, reading as

$$\begin{aligned}\mathcal{P}^{\text{int}}\left[\hat{v}_r^M(\varphi), \hat{v}_\varphi^M(\varphi)\right] = \\ -\int_{\varphi_b}^{\varphi_e} \left[\hat{v}_r^M(\varphi) + \frac{\mathrm{d}\hat{v}_\varphi^M(\varphi)}{\mathrm{d}\varphi}\right] n_\varphi(\varphi)\,\mathrm{d}\varphi \\ +\int_{\varphi_b}^{\varphi_e} \left[\frac{\mathrm{d}^2\hat{v}_r^M(\varphi)}{\mathrm{d}\varphi^2} - \frac{\mathrm{d}\hat{v}_\varphi^M(\varphi)}{\mathrm{d}\varphi}\right] \frac{m_z(\varphi)}{R}\,\mathrm{d}\varphi\,, \\ \forall\ \hat{v}_\varphi^M, \hat{v}_r^M \in \mathbb{R} \text{ with } \frac{\mathrm{d}\hat{v}_r^M(\varphi)}{\mathrm{d}\varphi}, \frac{\mathrm{d}\hat{v}_\varphi^M(\varphi)}{\mathrm{d}\varphi} \in \mathbb{R}\,,\end{aligned} \tag{16}$$

with shell-specific internal forces performing power on the midsurface-related virtual velocities. These internal forces are called circumferential normal forces (per length along the driving direction of the tunnel),

$$n_\varphi(\varphi) = \int_{R_{in}}^{R_{out}} \sigma_{\varphi\varphi}(r,\varphi)\,\mathrm{d}r\,, \tag{17}$$

and bending moments (per length in the driving direction of the tunnel),

$$m_z(\varphi) = \int_{R_{in}}^{R_{out}} \sigma_{\varphi\varphi}(r,\varphi) \times (r-R)\,\mathrm{d}r\,. \tag{18}$$

In order to use the Principle of Virtual Power according to Eq. (4), together with Eqs. (9) and (16), for deriving differential equations linking the force quantities n_φ, m_z, G_p, and G_s, Eqs. (9) and (16) need to be transformed in a way which provides the line integrals to comprise the functions $\hat{v}_\varphi^M(\varphi)$ and $\hat{v}_r^M(\varphi)$ (rather than their derivatives). This is realized through partial integration, which yields

$$\begin{aligned}\mathcal{P}^{\text{int}} = \int_{\varphi_{RI}}^{\varphi_{LI}} \left[-n_\varphi(\varphi) + \frac{\mathrm{d}^2 m_z(\varphi)}{R\,\mathrm{d}\varphi^2}\right] \hat{v}_r^M(\varphi)\,\mathrm{d}\varphi \\ -\left[\frac{\mathrm{d}m_z(\varphi)}{R\,\mathrm{d}\varphi}\right] \hat{v}_r^M(\varphi)\Big|_{\varphi_{RI}}^{\varphi_{LI}} + \left[\frac{m_z(\varphi)}{R}\right] \frac{\mathrm{d}v_r^M(\varphi)}{\mathrm{d}\varphi}\Big|_{\varphi_{RI}}^{\varphi_{LI}} \\ +\int_{\varphi_{RI}}^{\varphi_{LI}} \left[\frac{\mathrm{d}n_\varphi(\varphi)}{\mathrm{d}\varphi} + \frac{\mathrm{d}m_z(\varphi)}{R\,\mathrm{d}\varphi}\right] \hat{v}_\varphi^M(\varphi)\,\mathrm{d}\varphi \\ -\left[n_\varphi(\varphi) + \frac{m_z(\varphi)}{R}\right] \hat{v}_\varphi^M(\varphi)\Big|_{\varphi_{RI}}^{\varphi_{LI}},\end{aligned} \tag{19}$$

and

$$\begin{aligned}\mathcal{P}^{\text{ext}} = \int_{\varphi_{RI}}^{\varphi_{LI}} \left[\frac{h}{2}\frac{\mathrm{d}G_s(\varphi)}{\mathrm{d}\varphi} - R\,G_p(\varphi)\right] \hat{v}_r^M(\varphi)\,\mathrm{d}\varphi \\ +\int_{\varphi_{RI}}^{\varphi_{LI}} \left[R_o\,G_s(\varphi)\right] \hat{v}_\varphi^M(\varphi)\,\mathrm{d}\varphi - \left[\frac{h}{2}\,G_s(\varphi)\right] \hat{v}_r^M(\varphi)\Big|_{\varphi_{RI}}^{\varphi_{LI}} \\ +\ N_{RI}(\varphi)\left[\hat{v}_\varphi^M(\varphi_{RI})\right] - N_{LI}(\varphi)\left[\hat{v}_\varphi^M(\varphi_{LI})\right].\end{aligned} \tag{20}$$

Finally, insertion of Eqs. (19) and (20) into the principle of virtual power according to Eq. (4), and explicitly considering the arbitrariness of the functions $\hat{v}_\varphi^M(\varphi)$ and $\hat{v}_r^M(\varphi)$, yields differential equations along the entire tunnel shell segment, i.e. for $\varphi_{RI} \le \varphi \le \varphi_{LI}$,

$$\begin{aligned}-n_\varphi(\varphi) + \frac{\mathrm{d}^2 m_z(\varphi)}{R\,\mathrm{d}\varphi^2} - R\,G_p(\varphi) + \frac{h}{2}\frac{\mathrm{d}G_s(\varphi)}{\mathrm{d}\varphi} &= 0\,, \\ \frac{\mathrm{d}n_\varphi(\varphi)}{\mathrm{d}\varphi} + \frac{\mathrm{d}m_z(\varphi)}{R\,\mathrm{d}\varphi} + \left[R + \frac{h}{2}\right] G_s(\varphi) &= 0\,,\end{aligned} \tag{21}$$

as well as the natural boundary conditions valid at the right and the left impost of the tunnel shell segment representing the top heading. Mathematically, these natural boundary conditions read as

$$\text{for } i = RI, LI:$$

$$-\frac{1}{R}\frac{\mathrm{d}m_z}{\mathrm{d}\varphi}(\varphi_i) - G_s(\varphi_i) \times \frac{h}{2} = 0\,, \tag{22}$$

$$m_z(\varphi_i) = 0\,, \tag{23}$$

$$-n_\varphi(\varphi_i) - N_i = 0\,. \tag{24}$$

The physical meaning of Eq. (22) can be formulated as follows: In order to equilibrate an external ground shear traction acting half the shell thickness off the shell's mid-surface, the internal bending moment around the driving direction per length in driving direction needs to change along the tunnel circumference.

The physical meaning of Eq. (23) can be formulated as follows: Vanishing external bending moments at the impost imply an internal moment distribution with a tendency to zero towards the impost location.

In order to obtain mathematical solutions for the differential equations (21), Eq. $(21)_2$ is first differentiated with respect to φ, and the

corresponding result is then solved for $\mathrm{d}^2 m_z/(R\,\mathrm{d}\varphi^2)$. This yields

$$\frac{\mathrm{d}^2 m_z(\varphi)}{R\,\mathrm{d}\varphi^2} = -\frac{\mathrm{d}^2 n_\varphi(\varphi)}{\mathrm{d}\varphi^2} - \left[R + \frac{h}{2}\right]\frac{\mathrm{d}G_s(\varphi)}{\mathrm{d}\varphi}\,. \tag{25}$$

Re-insertion of Eq. (25) into Eq. $(21)_1$ results in a differential equation for the normal force n_φ, reading as

$$n_\varphi(\varphi) + \frac{\mathrm{d}^2 n_\varphi(\varphi)}{\mathrm{d}\varphi^2} = -R\,\frac{\mathrm{d}G_s(\varphi)}{\mathrm{d}\varphi} - R\,G_p(\varphi)\,. \tag{26}$$

4. Normal force and bending moment distributions resulting from ground-induced external loads

The differential equation (26) can be readily solved for the boundary conditions according to Eq. (24) and for traction forces exerted from the ground onto the tunnel shell. These forces are represented by polynomial functions. The degree of these polynomials is chosen according to the type of available geodetic displacement data. In the present case, cubic polynomials for the normal traction force distributions, with four ground pressure values $G_{p,i}$, $i = 1,2,3,4$, see Fig. 1(a), are appropriate. Mathematically speaking, this reads as

$$\begin{aligned} G_p(\bar\varphi) = {} & A_1(\bar\varphi)\,G_{p,1} + A_2(\bar\varphi)\,G_{p,2} \\ + {} & A_3(\bar\varphi)\,G_{p,3} + A_4(\bar\varphi)\,G_{p,4}\,, \end{aligned} \tag{27}$$

where the inclined azimuthal coordinate $\bar\varphi = \varphi - \varphi_{RI}$, is measured from the right impost of the tunnel segment, where $G_{p,1}$ is the pressure at position $\bar\varphi = 0$, $G_{p,2}$ is the pressure at position $\bar\varphi = \Delta\varphi/3$, $G_{p,3}$ is the pressure at position $\bar\varphi = 2\Delta\varphi/3$, and $G_{p,4}$ is the pressure at position $\bar\varphi = \Delta\varphi$, see Figs. 1 and 2, where $\Delta\varphi = \varphi_{LI} - \varphi_{RI}$ is the opening angle of the tunnel shell, $\Delta\bar\varphi = 2.92$ rad, see Fig. 1. Moreover, the cubic polynomials A_i, with $i = 1,2,3,4$, read as

$$\begin{aligned} A_1(\bar\varphi) &= 1 - \frac{11\bar\varphi}{2\Delta\varphi} + \frac{9\bar\varphi^2}{(\Delta\varphi)^2} - \frac{9\bar\varphi^3}{2(\Delta\varphi)^3}\,, \\ A_2(\bar\varphi) &= \frac{9\bar\varphi}{\Delta\varphi} - \frac{45\bar\varphi^2}{2(\Delta\varphi)^2} + \frac{27\bar\varphi^3}{2(\Delta\varphi)^3}\,, \\ A_3(\bar\varphi) &= -\frac{9\bar\varphi}{2\Delta\varphi} + \frac{18\bar\varphi^2}{(\Delta\varphi)^2} - \frac{27\bar\varphi^3}{2(\Delta\varphi)^3}\,, \\ A_4(\bar\varphi) &= \frac{\bar\varphi}{\Delta\varphi} - \frac{9\bar\varphi^2}{2(\Delta\varphi)^2} + \frac{9\bar\varphi^3}{2(\Delta\varphi)^3}\,, \end{aligned} \tag{28}$$

see Figs. 2(a)–(d). Shear traction forces are considered to be activated only in the regions close to the imposts, with distributions reading as

$$G_s(\bar\varphi) = A_1(\bar\varphi)\,G_{s,1} + A_4(\bar\varphi)\,G_{s,4}\,, \tag{29}$$

whereby $G_{s,1}$ is the shear at position $\bar\varphi = 0$, and $G_{s,4}$ is the shear at position $\bar\varphi = \Delta\varphi$; see Fig. 1 for the positions of the ground shear intensities, and Fig. 2 for illustration of ground traction distributions and involved cubic polynomials.

The corresponding normal force distribution, which solves Eq. (26) for the boundary conditions according to Eq. (24) and for the ground actions according to Eqs. (27) and (29), together with Eq. (28), reads as

$$\begin{aligned} n_\varphi(\bar\varphi) = {} & N_{RI}\,\mathcal{I}_{RI\to f}(\bar\varphi) \\ + {} & N_{LI}\,\mathcal{I}_{LI\to f}(\bar\varphi) \\ - {} & \textstyle\sum_{i=1}^{4} R\,G_{p,i}\,\mathcal{I}_{p,i\to f}(\bar\varphi) \\ + {} & \textstyle\sum_{i\in[1,4]}\left[R - \frac{h}{2}\right] G_{s,i}\,\mathcal{I}_{s,i\to f}(\bar\varphi)\,, \end{aligned} \tag{30}$$

with azimuthal influence functions $\mathcal{I}$ quantifying the influence of impost forces and of ground pressure and shear values, on the internal normal force distribution; mathematically, they are given through Eqs. (73)–(78) and (81)–(82) of Appendix.

Solution of the differential equation $(21)_2$, by simple integration, for the boundary condition according to Eq. (23), with $i = RI$, for the normal forces according to Eq. (30), and for the distribution of the shear traction forces according to Eq. (29), yields

$$\begin{aligned} m_z(\bar\varphi) = {} & R\,N_{RI}\left[1 - \mathcal{I}_{RI\to f}(\bar\varphi)\right] \\ - {} & R\,N_{LI}\,\mathcal{I}_{LI\to f}(\bar\varphi) \\ + {} & \textstyle\sum_{i=1}^{4} R^2\,G_{p,i}\,\mathcal{I}_{p,i\to f}(\bar\varphi) \\ + {} & \textstyle\sum_{i\in[1,4]}\left[R^2\right] G_{s,i}\,\mathcal{I}_{s,i\to m}(\bar\varphi) \\ - {} & \textstyle\sum_{i\in[1,4]}\left[R^2 - \frac{R\,h}{2}\right] G_{s,i}\,\mathcal{I}_{s,i\to f}(\bar\varphi)\,, \end{aligned} \tag{31}$$

with azimuthal influence functions $\mathcal{I}$ quantifying the influence of impost forces and of ground pressure and shear values, on the internal bending moment distribution; mathematically, they are given through Eqs. (73)–(82) of the Appendix.

Eq. (31), together with three natural boundary conditions, given through Eq. (22) with $i = LI, RI$ and Eq. (23) with $i = LI$, allows for the derivation of three equations supporting the displacement-to-external force translation scheme of Section 6. In more detail, the natural boundary equation according to Eq. (22), with $i = RI$ and $i = LI$, specified for the bending moment according to Eq. (31) and for the shear traction forces according to Eq. (29), yields

$$\begin{aligned} 0 = {} & -N_{RI}\,\frac{1}{\tan(\Delta\varphi)} + N_{LI}\,\frac{1}{\sin(\Delta\varphi)} \\ & + \textstyle\sum_{i\in[1,4]} G_{s,i}\left[\left(R - \frac{h}{2}\right)\mathcal{I}_{s,i\to RI}(\bar\varphi = 0)\right] \\ & + \textstyle\sum_{i=1}^{4} R\,G_{p,i}\,\mathcal{I}_{p,i\to RI}(\bar\varphi = 0) + R\,G_{s,1}\,, \end{aligned} \tag{32}$$

and

$$\begin{aligned} 0 = {} & -N_{RI}\,\frac{1}{\sin(\Delta\varphi)} + N_{LI}\,\frac{1}{\tan(\Delta\varphi)} \\ & + \textstyle\sum_{i\in[1,4]} G_{s,i}\left[\left(R - \frac{h}{2}\right)\mathcal{I}_{s,i\to LI}(\bar\varphi = \Delta\varphi)\right] \\ & + \textstyle\sum_{i=1}^{4} R\,G_{p,i}\,\mathcal{I}_{p,i\to LI}(\bar\varphi = \Delta\varphi) + R\,G_{s,4}\,, \end{aligned} \tag{33}$$

with azimuthal influence functions $\mathcal{I}$, as given through Eqs. (107)–(118) of the Appendix. Specification of the natural boundary condition according to Eq. (23) with $i = LI$, for the bending moment according to Eq. (31), yields

$$N_{RI} - N_{LI} - G_{s,1}\,R\,\Delta\varphi/8 - G_{s,4}\,R\,\Delta\varphi/8 = 0\,. \tag{34}$$

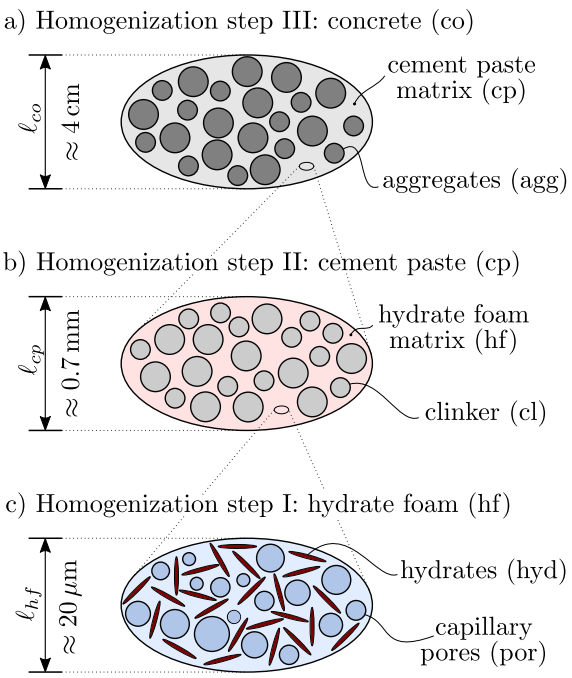

Fig. 3. Micromechanical modeling of concrete, according to [44–46]: two-dimensional sketches of three-dimensional representative volume elements.

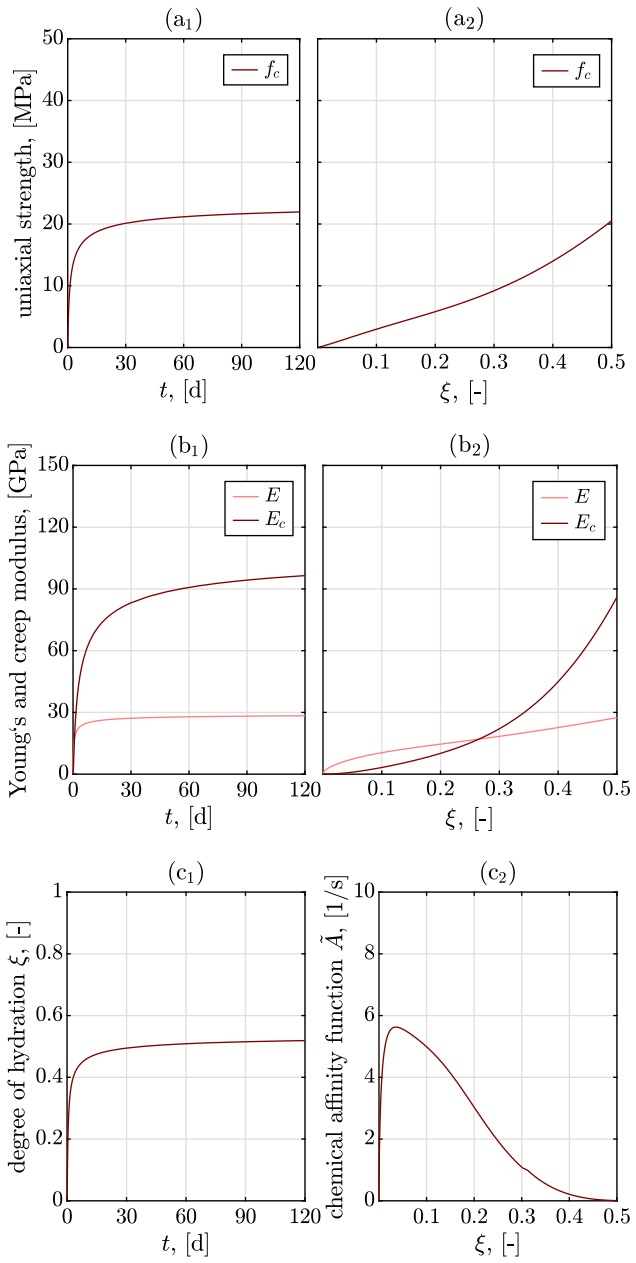

Fig. 4. Hydration-driven material properties of shotcrete, based on hierarchical micromechanics model [44] and relevant standards [47]: (a_1) isothermal strength evolution at 20 centigrades, (a_2) shotcrete strength as function of hydration degree, (b_1) isothermal elastic and creep modulus evolution at 20 centigrades, (b_2) shotcrete elastic and creep modulus as function of hydration degree, (c_1) isothermal hydration degree evolution at 20 centigrades, (c_2) chemical affinity function for shotcrete hydration.

It is noted that Eqs. (32)–(34) are equilibrium conditions involving external forces only. Remarkably, equivalent information may be obtained from the principle of virtual power evaluated for virtual rigid body movements $\hat{\mathbf{v}}^{RB}$, with consideration of $\mathcal{P}^{\text{int}}(\hat{\mathbf{v}}^{RB}) = 0$.

5. Deformations of aging viscoelastic shells loaded by ground pressure and shear

As detailed in [16,17], the virtual velocity field of Eq. (5) is used to approximate the circumferential normal strains in the tunnel shell. First, it is recalled that the virtual strain field associated with the velocity field of Eq. (5) is very simple and exhibits only one component, namely the circumferential normal one, which follows the classical relation [34], p. 747,

$$\hat{d}_{\varphi\varphi} = \frac{1}{r}\frac{\partial \hat{v}_\varphi}{\partial \varphi} + \frac{\hat{v}_r}{r}\,. \tag{35}$$

Insertion of Eq. (5) into (35), followed by a variable change from midsurface virtual velocities to midsurface (small) displacements, $\hat{v}_r^M \rightarrow u_r^M$, $\hat{v}_\varphi^M \rightarrow u_\varphi^M$, and from virtual circumferential normal strain rates to actual circumferential normal strains, $\hat{d}_{\varphi\varphi} \rightarrow \varepsilon_{\varphi\varphi}$, yields an expression for the circumferential normal strain field, which reads as [16]

$$\varepsilon_{\varphi\varphi}(r,\varphi) = \frac{1}{r}u_r^M(\varphi) + \frac{1}{R}\frac{\mathrm{d}u_\varphi^M(\varphi)}{\mathrm{d}\varphi} - \frac{r-R}{rR}\frac{\mathrm{d}^2 u_r^M(\varphi)}{\mathrm{d}\varphi^2}\,. \tag{36}$$

These normal strains are then seen as the result of the action of the normal circumferential stresses, via a nonlinear aging viscoelastic material law of the format [17,48]

$$\dot{\varepsilon}_{\varphi\varphi}(t) = \left(1-\nu^2\right)\int_0^t \frac{\partial \boldsymbol{J}^\sigma}{\partial t}\left(\xi(t),\eta(t),t-\tau\right)\dot{\sigma}_{\varphi\varphi}(\tau)\,\mathrm{d}\tau\,, \tag{37}$$

whereby t denotes the current time instant, τ denotes (past) time instances of stress application, ν denotes the (isotropic) Poisson's ratio, which is classically defined as the negative ratio of radial-over-circumferential normal strains arising from uniaxial circumferential stress states; for concrete, it typically amounts to $\nu = 0.2$. It is noted in passing that isotropic viscoelasticity implies the radial normal strains to evolve as

$$\varepsilon_{rr} = \frac{\nu}{1+\nu}\,\varepsilon_{\varphi\varphi}\,. \tag{38}$$

This type of deformation is considered inessential for equilibrium, since $\hat{d}_{rr} \equiv 0$, in accordance with Eq. (5). In Eq. (37), J^σ denotes the uniaxial creep function for highly stressed concrete, which for the current application range, can be suitably approximated by a power-law function which reads as [17,49–52],

$$\begin{aligned} &\boldsymbol{J}^\sigma\left(\xi(t),\eta(t),t-\tau\right) = \\ &= H(t-\tau)\left[\frac{1}{E\left(\xi(t)\right)} + \frac{\eta(t)}{E_c\left(\xi(t)\right)}\left(\frac{t-\tau}{t_0^*}\right)^\beta\right], \end{aligned} \tag{39}$$

with Heaviside function H, the elastic Young's modulus E, the degree of hydration ξ, the creep affinity coefficient η considering non-linear creep, the creep modulus E_c, and the creep exponent amounting to $\beta \approx 0.25$ [53,54], when determined together with a reference time of $t_0^* = 1\text{d}$.

Generally speaking, the first law of thermodynamics in combination with a chemical kinetics law for the hydration of concrete may enter a thermochemical analysis [55], with fields of temperature and hydration degree as a results. The latter may then enter multiscale material models of concrete, as depicted in Fig. 3. Being based on material-invariant (micro-)creep and (micro-)strength properties of the reactants between water and cement, standardly called hydrates, as well as on the (micro-)elastic properties of aggregates, clinker and hydrates, such micromechanical models translate hydration degree and mixture characteristics, namely the water-to-cement ratio and the aggregate-to-cement ratio, into elastic, creep, and strength properties at the cement paste and concrete scale [44,45,54].

Going more into detail, a piece of material is considered as a representative volume element (RVE), which is subjected to homogeneous "macroscopic" strains [56] and which consists of different quasi-homogeneous subdomains called material phases [57]. Each of these phases may qualify as yet another RVE at a lower scale [58], as seen in Fig. 3: An RVE of concrete consists of the phases "cement paste" and "aggregates", see Fig. 3(a), cement paste qualifies as yet another RVE, depicted in Fig. 3(b), with the phases "clinker" and "hydrate foam matrix", and the hydrate foam appears, at a yet smaller scale, as an RVE consisting of the phases "hydrates" and "capillary pores", see Fig. 3(c). Creep behavior is suitably upscaled in terms of relaxation

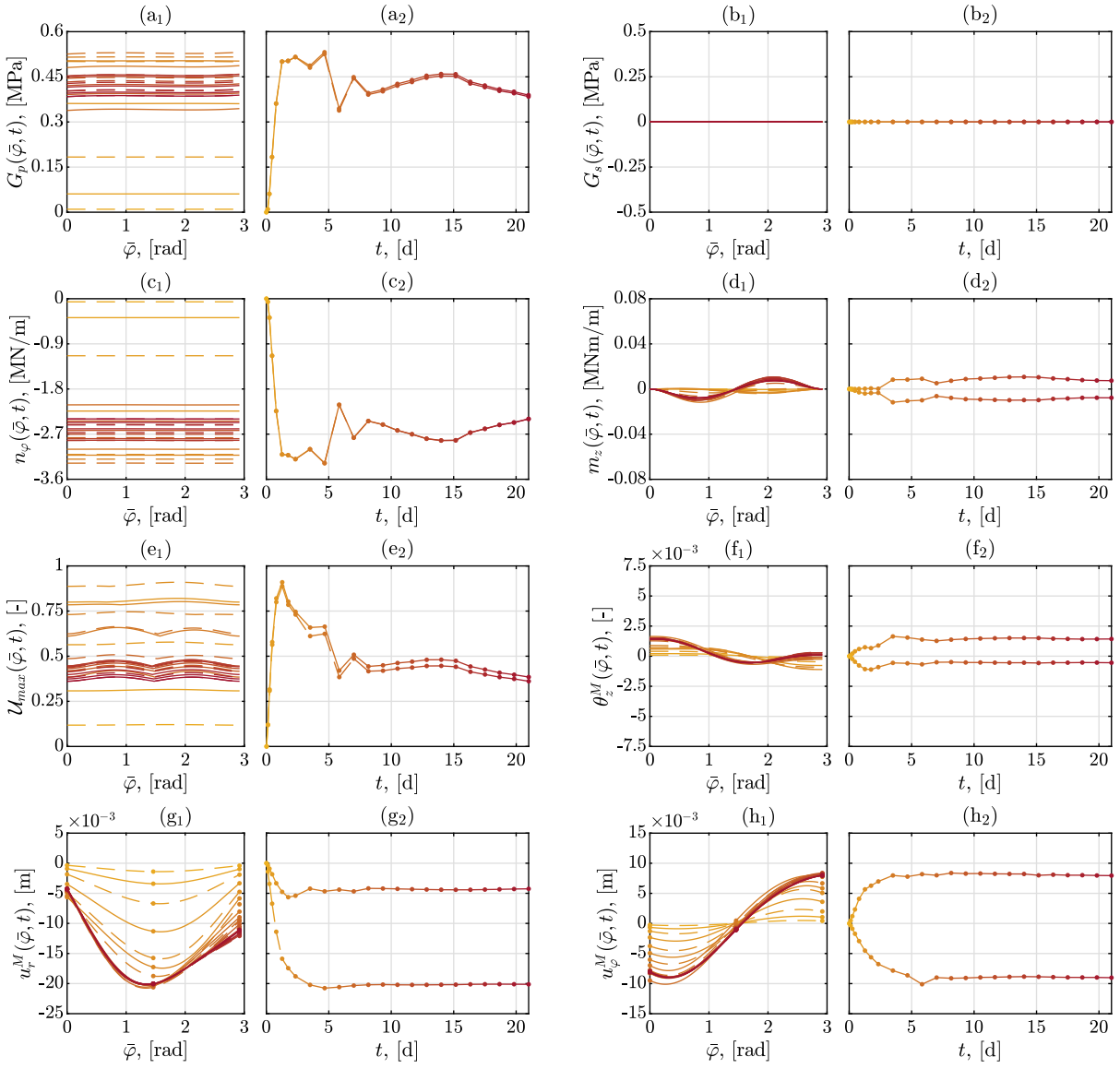

Fig. 5. Structural behavior of NATM tunnel without shell-to-ground shear transfer ($k_{s,p} = 0$): Distribution of ground pressure (a), shear traction forces (b), circumferential normal forces (c), bending moments (d), maximum degree of utilization (e), generator rotations (f), as well as radial and circumferential displacements (g-h) along the circumference of the top heading of Sieberg tunnel (index 1), and the temporal evolution of maximum and minimum values (index 2).

functions, and the relation between creep and relaxation functions becomes particularly compact in the Laplace–Carson space [48,59,60]. The Laplace–Carson transform $\mathcal{L}_C$ assigns to function of the time variable t, a function of a frequency-type variable p, according to

$$\mathcal{L}_C\{f(t)\} = F^*(p) = p\int_0^\infty e^{-pt} f(t)\,dt\,, \tag{40}$$

and in the Laplace–Carson space, fourth-order creep and relaxation tensors, denoted as $\mathbf{J}$ and $\mathbf{R}$ are related by [48,59,60]

$$\mathbf{J}^*(p) = \mathbf{R}^*(p)^{-1}\,. \tag{41}$$

The relaxation properties of the hydrate phase in an RVE of hydrate foam, as depicted in Fig. 3(c), are represented by tensor $\mathbf{R}_{hyd}^{hf,*}(p)$, see [54] for details. They are upscaled to that of concrete by means of a sequential homogenization procedure according to [54]

$$\mathbf{R}_{hf}^{cp,*}(p) = f_{hyd}^{hf}\,\mathbf{R}_{hyd}^{hf,*}(p) : \mathbf{A}_{hyd}^{hf,*}(p)\,, \tag{42}$$

$$\begin{aligned}\mathbf{R}_{cp}^{co,*}(p) = {} & f_{hf}^{cp}\,\mathbf{R}_{hf}^{cp,*}(p) : \mathbf{A}_{hf}^{cp,*}(p) \\ & + f_{cl}^{cp}\,\mathbf{R}_{cl}^{cp,*} : \mathbf{A}_{cl}^{cp,*}(p)\,,\end{aligned} \tag{43}$$

$$\begin{aligned}\mathbf{R}_{co}^{*}(p) = {} & f_{cp}^{co}\,\mathbf{R}_{cp}^{co,*}(p) : \mathbf{A}_{cp}^{co,*}(p) \\ & + f_{ag}^{co}\,\mathbf{R}_{ag}^{co,*} : \mathbf{A}_{agg}^{co,*}(p)\,,\end{aligned} \tag{44}$$

with $\mathbf{R}_r^s$, $r = hyd, hf, cl, cp, agg$, $s = hf, cp, co$, denoting the relaxation tensor of phase r in RVE s, with $\mathbf{R}_{co}$ as the relaxation tensor of concrete, with $\mathbf{A}_r^s$ denoting the concentration or downscaling tensor of phase r in RVE s, and with f_i^j as the volume fractions of phase i in RVE j, all depending on the hydration degree and the water-to-cement and aggregate-to-cement ratio, as given in more in detail in [44]. It is noted that aggregates, clinker, and pores behave fully elastically, so that the relaxation tensors do not depend on variable p and are actually identical to the stiffness tensors, while the stiffness of the pores vanishes as drained conditions prevail [54]. Moreover, the concentration tensors of hydrate foam, clinker, cement paste, and aggregates follow from the so-called Mori–Tanaka–Benveniste scheme for composite materials [61–63], while the concentration tensor of hydrates follows from the self-consistent homogenization scheme for polycrystals [57,64–67]. The upscaling scheme according to Eqs. (42)–(44) naturally comprises the limit case of pure elasticity upscaling, through identifying the elastic

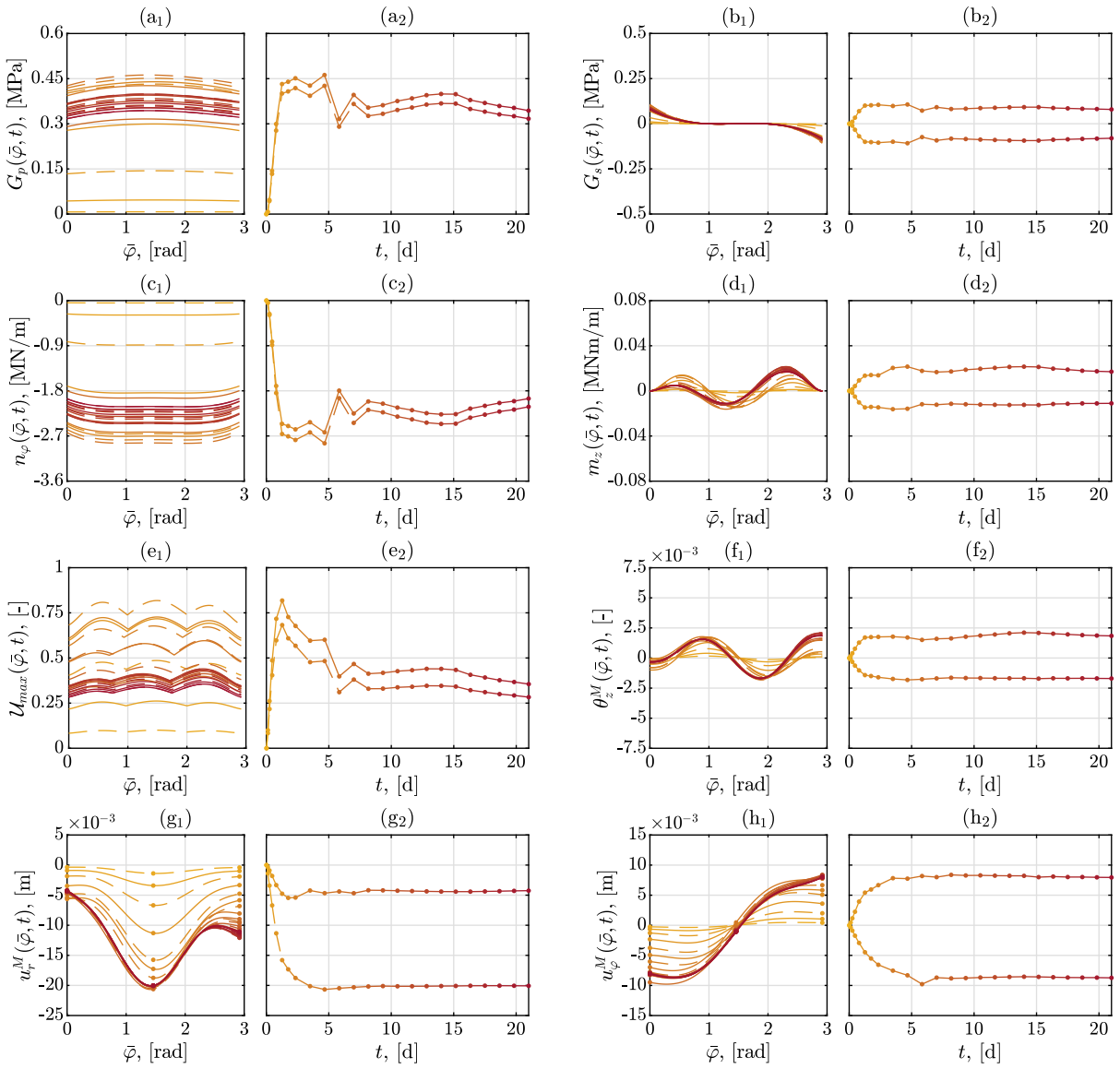

Fig. 6. Structural behavior of NATM tunnel with low shell-to-ground shear transfer ($k_{s,p} = 0.25$): Distribution of ground pressure (a), shear traction forces (b), circumferential normal forces (c), bending moments (d), maximum degree of utilization (e), generator rotations (f), as well as radial and circumferential displacements (g-h) along the circumference of the top heading of Sieberg tunnel (index 1), and the temporal evolution of maximum and minimum values (index 2).

stiffness tensor $\mathbf{C}$ as the relaxation tensor evaluated at time zero, i.e.

$$\mathbf{R}_i(t=0) = \mathbf{C}_i, \qquad i = hyd, cl, co, \tag{45}$$

together with trivial identities for the purely elastic phases,

$$\mathbf{R}_i = \mathbf{C}_i, \qquad i = cl, agg. \tag{46}$$

Under pseudo-isothermal conditions, as adopted here, a short-cut based on code-related formulae may be adopted. Then, the temporal evolution under isothermal conditions at 20 °C is approximated by a suitable fitting function, through [47,53]

$$E(t) = E_{28d}\left\{\exp\left[s_E\left(1-\sqrt{\frac{28\,\text{days}}{t}}\right)\right]\right\}^{0.5}, \tag{47}$$

with $E_{28\text{d}}$ as the 28 day value of elastic modulus of shotcrete,

$$E_{28d} = 21.5\,\text{GPa}\times\alpha\left(\frac{f_{c,28d}}{f_c^*}\right)^{1/3}. \tag{48}$$

In the context of Sieberg tunnel [17], cement type CEM II/A-S 42.5R implies the evolution parameter s_E to amount to 0.18, strength class SpC20/25 implies the 28 day value of uniaxial compressive strength of shotcrete $f_{c,28\text{d}}$ to amount to 20 MPa; furthermore, the reference strength level is $f_c^* = 10$ MPa, and for quartz or limestone aggregate, the parameter for the stiffness of the aggregates α is equal to one. The creep modulus E_c is available from isothermal creep tests performed at a temperature of 20 centigrades [47,53],

$$E_c(t) = E_{c,28d}\left\{\exp\left[s_{E_c}\left(1-\sqrt{\frac{28\,\text{days}}{t}}\right)\right]\right\}^{0.5}, \tag{49}$$

with $E_{c,28\text{d}}$ as the 28 day value of creep modulus of shotcrete,

$$E_{c,28d} = 51.9\,\text{GPa}\times\alpha^2\left(\frac{f_{c,28d}}{f_c^*}\right)^{2/3}. \tag{50}$$

Moreover, cement type CEM II/A-S 42.5R implies the evolution parameter to amount to $s_{E_c} = 0.61$. The affinity factor η is left to be quantified, more precisely $\eta\left(\bar{\sigma}_{\varphi\varphi}(\varphi,t), \bar{\sigma}_{zz}(\varphi,t)\right)$, which depends on the circumferential and axial normal stresses averaged over the shell thickness [17], $\bar{\sigma}_{\varphi\varphi}$ and $\bar{\sigma}_{zz}$, and which is linked to the stress-over-strength ratio or utilization degree $\mathcal{U}$ (> 0), via [68]

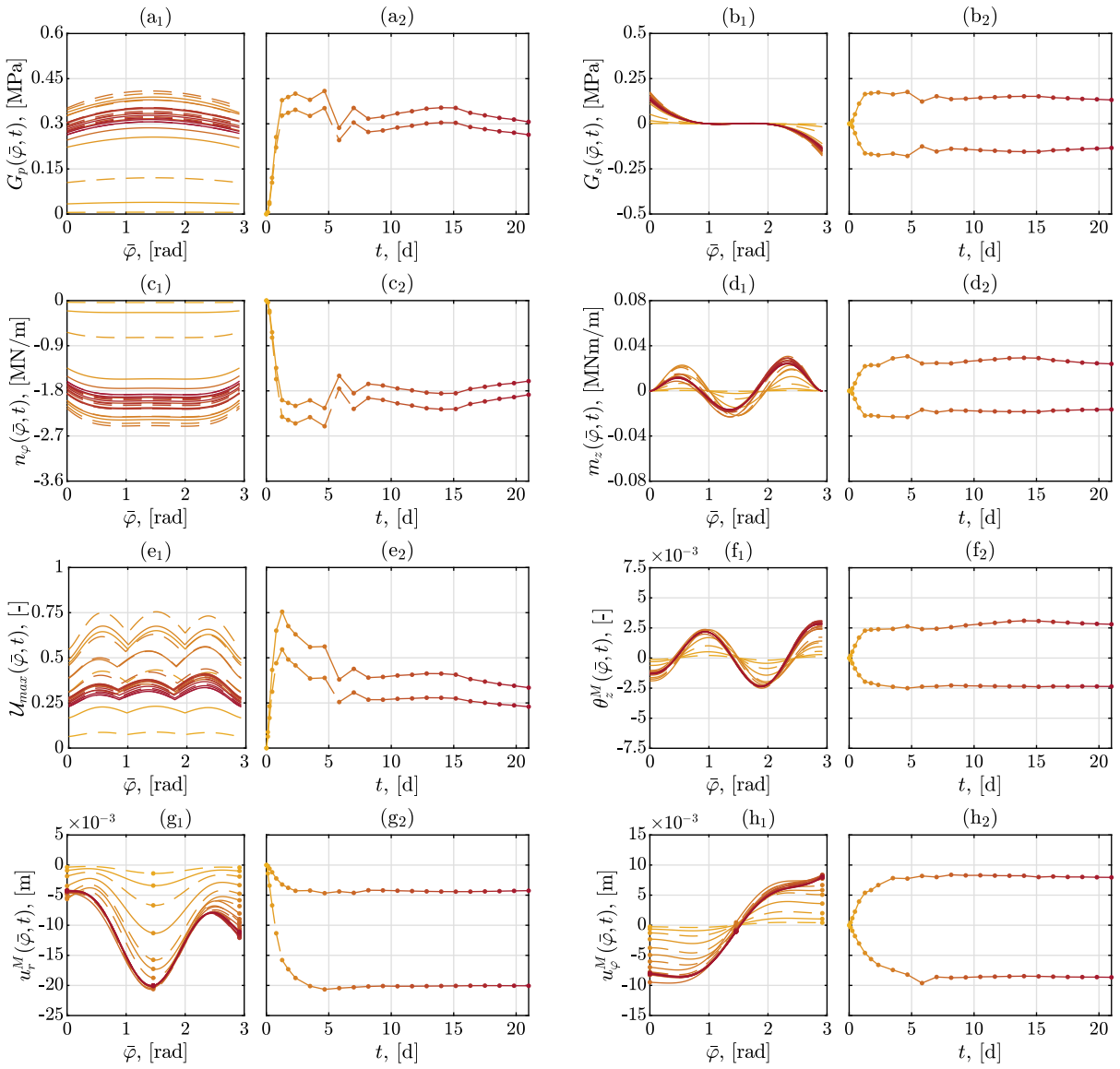

Fig. 7. Structural behavior of NATM tunnel with medium shell-to-ground shear transfer ($k_{s,p} = 0.50$): Distribution of ground pressure (a), shear traction forces (b), circumferential normal forces (c), bending moments (d), maximum degree of utilization (e), generator rotations (f), as well as radial and circumferential displacements (g-h) along the circumference of the top heading of Sieberg tunnel (index 1), and the temporal evolution of maximum and minimum values (index 2).

$$\eta(\varphi,t) = 1 + 2\,\left(\mathcal{U}[\bar{\sigma}_{\varphi\varphi}(\varphi,t),\bar{\sigma}_{zz}(\varphi,t)]\right)^4 . \tag{51}$$

In order to define $\mathcal{U}$ in a general three-dimensional setting, a Drucker–Prager strength criterion [69] is adopted. This criterion is specified for the stress components occurring in the tunnel shell, so that

$$\begin{aligned}\mathcal{U}(r,\varphi,t) = &\ \frac{\alpha_{DP}}{k_{DP}}\left[\sigma_{\varphi\varphi}(r,\varphi,t)+\sigma_{zz}(r,\varphi,t)\right]\\ &+\ \frac{1}{k_{DP}}\left\{\frac{2}{3}\left[\left(\sigma_{\varphi\varphi}(r,\varphi,t)\right)^2-\sigma_{\varphi\varphi}(r,\varphi,t)\right.\right.\\ &\left.\left.\times\ \sigma_{zz}(r,\varphi,t)+\left(\sigma_{zz}(r,\varphi,t)\right)^2\right]\right\}^{1/2},\end{aligned} \tag{52}$$

with parameters α_{DP} and k_{DP} being related to the uniaxial and biaxial compressive strengths of shotcrete, denoted as f_c and f_b,

$$\alpha_{DP} = \sqrt{\frac{2}{3}}\,\frac{\kappa-1}{2\kappa-1}, \qquad k_{DP} = \sqrt{\frac{2}{3}}\left[1-\frac{\kappa-1}{2\kappa-1}\right] f_c\,, \tag{53}$$

where the strength ratio $\kappa = f_b/f_c = 1.15$ follows from classical mechanical experiments [70]. In analogy to the relations for elasticity and creep, which are given in Eqs. (47) and (49), the temporal evolution of the uniaxial strength of shotcrete under isothermal conditions at 20 centigrade can be approximated according to relevant standards [47],

$$f_c(t) = f_{c,28\mathrm{d}}\,\exp\left[s_E\left(1-\sqrt{\frac{28\,\mathrm{days}}{t}}\right)\right]. \tag{54}$$

Finally, bending moments and normal forces according to Eqs. (30) and (31) provide access to axial and circumferential normal stress tensor components, via [16,17,71]

$$\sigma_{\varphi\varphi}(r,\bar{\varphi}) = \frac{n_\varphi(\bar{\varphi})}{h} + \frac{12\,m_z(\bar{\varphi})}{h^3}\,(r-R)\,, \tag{55}$$

$$\sigma_{zz}(r,\bar{\varphi}) = \nu\,\sigma_{\varphi\varphi}(r,\bar{\varphi})\,. \tag{56}$$

The issues of utilization degree and strength deserve a few comments in light of the multiscale scheme depicted in Fig. 3. The hierarchical micromechanics model for concrete strength reported in [44] combines two essential steps for downscaling macrostresses at the concrete level, i.e. subjected to the RVE seen in Fig. 3(a), down to microstresses at the hydrate level, i.e. stresses associated with the phase indicated in Fig. 3(c). At the hydrate scale, material failure is

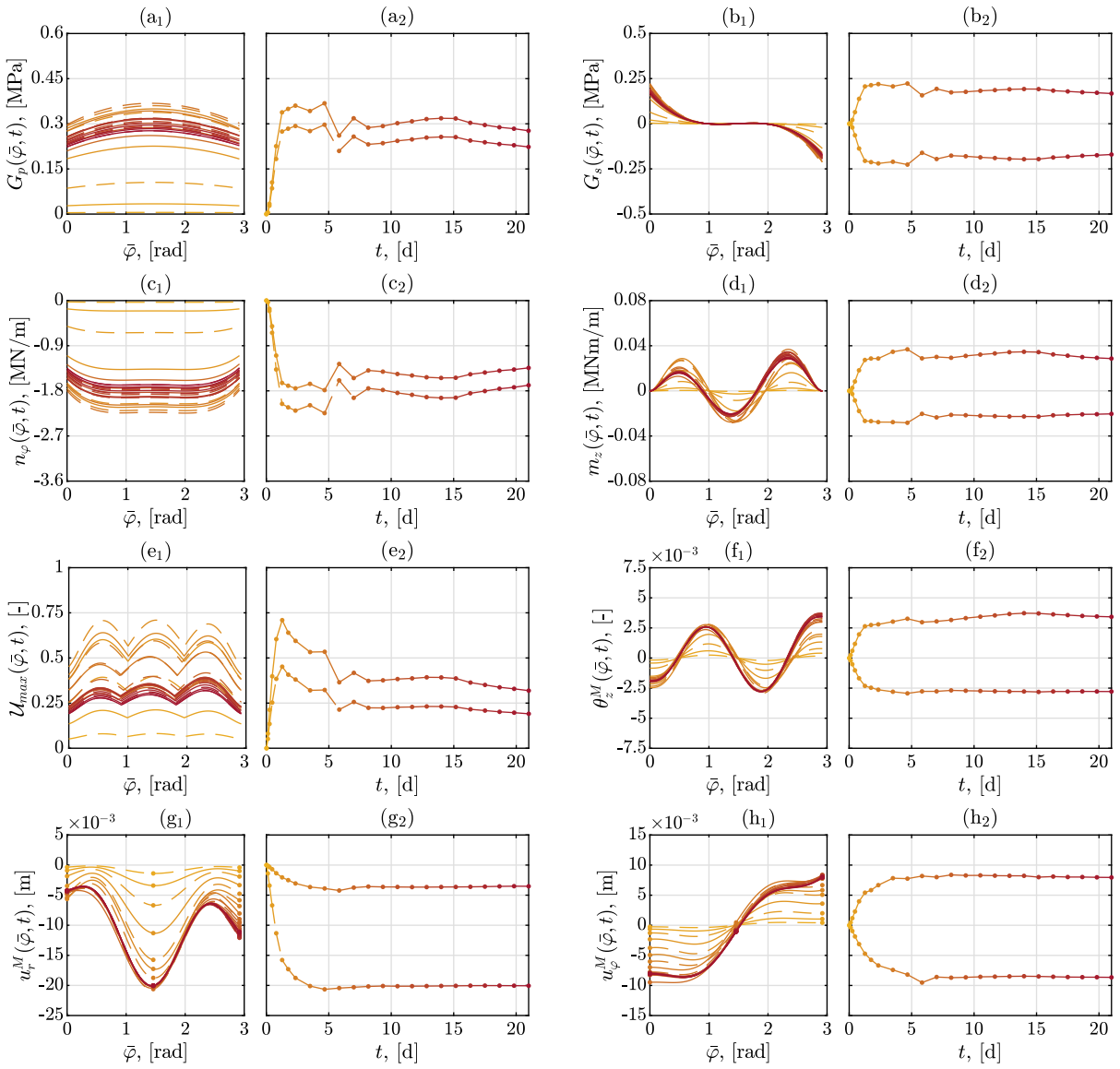

Fig. 8. Structural behavior of NATM tunnel with high shell-to-ground shear transfer ($k_{s,p} = 0.75$): Distribution of ground pressure (a), shear traction forces (b), circumferential normal forces (c), bending moments (d), maximum degree of utilization (e), generator rotations (f), as well as radial and circumferential displacements (g-h) along the circumference of the top heading of Sieberg tunnel (index 1), and the temporal evolution of maximum and minimum values (index 2).

initiated, according to a Mohr–Coulomb failure law reflecting nanoindentation hardness measurements [72,73]. The first downscaling step concerns the transition from the concrete level to the cement paste in the immediate vicinity of the aggregates, i.e. the interfacial transition zone (ITZ) [74]. This downscaling is realized through combination of a Mori–Tanaka–Benveniste scheme with traction and displacement continuity requirements at the interface between aggregate and cement paste [75,76]. The second downscaling step, from the cement paste in the ITZ down to the hydrates therein, employs higher-order averages [77,78] for identification of failure-inducing stress states at the hydrate scale, identifying these averages from derivatives of larger-scale stiffness properties [45]. Conclusively, the hierarchical micromechanics model for concrete strength reported in [44] establishes a relation between the hydration degree and the uniaxial strength of concrete, depicted for a water-to-cement ratio of 0.50 and an aggregate volume fraction of 0.7 per volume of concrete, in Fig. 4 (a_2). Comparing this relation with the isothermal strength evolution according to Eq. (54), depicted in Fig. 4 (a_1), allows for re-constructing the isothermal evolution of the hydration degree, which underlies the shotcrete development. It is depicted in Fig. 4 (c_1), again for a water-to-cement ratio of 0.50 and an aggregate volume fraction of 0.70 per volume of concrete. Comparing this hydration degree evolution with those of the elastic and creep moduli, depicted in Fig. 4 (b_1), yields material functions for the latter, see Fig. 4 (b_2). They are fully consistent with material functions obtained from direct experimental observations [50]. Finally, the isothermal hydration degree evolution gives access to the chemical affinity function [79,80]

$$\tilde{A}[\xi_{iso}(t)] = \dot{\xi}_{iso}(t)\exp\left(\frac{E_a}{RT}\right) \rightarrow \tilde{A}(\xi)\,, \tag{57}$$

with the ratio of activation energy and ideal gas constant amount to roughly $E_a/R \approx 4000\,\mathrm{K}$ [81]; see Fig. 4 (c_2) for the chemical affinity function associated with the shotcrete mixture introduced further above and underlying all computations given in the present paper. This function would allow for extension of the currently reported results to the non-isothermal case, e.g. in the context of nonlinear thermochemical finite element analyses [55].

With the constitutive framework for shotcrete mechanics modeling being set now, it is time to return to the level of the tunnel shell, and

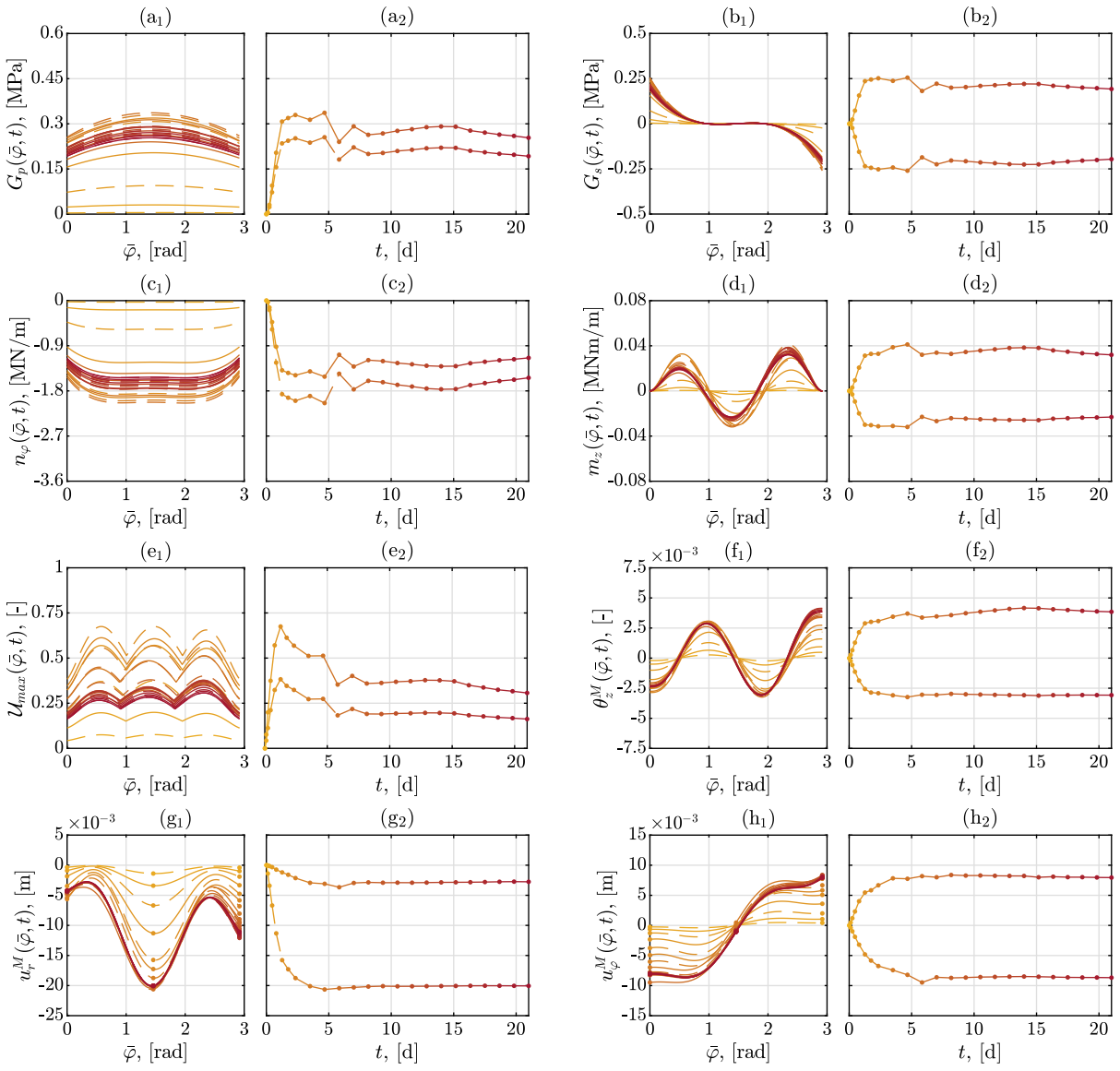

Fig. 9. Structural behavior of NATM tunnel with very high shell-to-ground shear transfer ($k_{s,p}$ = 1.00): Distribution of ground pressure (a), shear traction forces (b), circumferential normal forces (c), bending moments (d), maximum degree of utilization (e), generator rotations (f), as well as radial and circumferential displacements (g-h) along the circumference of the top heading of Sieberg tunnel (index 1), and the temporal evolution of maximum and minimum values (index 2).

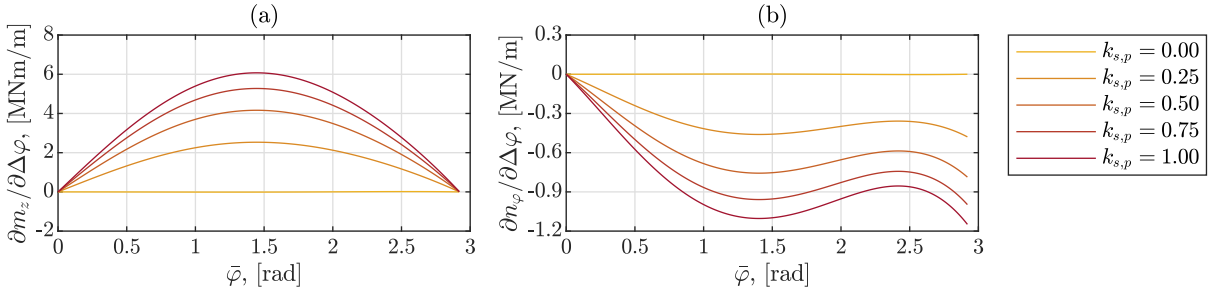

Fig. 10. Influence of geometrical change in terms of opening angle ("introduction of asymmetry") on internal force distribution: (a) bending moment, (b) circumferential normal force; in dependence of the shear-to-normal ground traction ratio $k_{s,p}$.

therefore integrate the circumferential strains according to Eq. (37), via Eqs. (17) and (18), to circumferential normal forces n_φ and bending moments around the longitudinal direction, m_z. This yields differential equations for $u_r^M(\varphi,t)$ and $u_\varphi^M(\varphi,t)$. These differential equations can be solved for the loading patterns quantified through Eq. (24) as well as Eqs. (27)–(29), yielding displacement rates as function of circumferential position and time. These differential equations are complemented by a differential equation for generator rotations θ_z^M. The latter are

obtained from derivation of the radial displacement component with respect to the circumferential midsurface line. Mathematically speaking, the aforementioned three differential equations are as follows: The radial displacement component rates fulfill

$$\begin{aligned}
&+\dot{u}_r^M(\bar{\varphi},t) - \dot{u}_r^{\mathrm{MP3}}(t)\cos(\bar{\varphi}) - \dot{u}_\varphi^{\mathrm{MP3}}(t)\sin(\bar{\varphi})\\
&-R\,\dot{\theta}_{z,RI}^M(t)\sin(\bar{\varphi})\\
&= \mathcal{I}_{RI\to r}(\bar{\varphi})\left[\int_0^t \frac{\partial J^\sigma}{\partial t}\,\dot{N}_{RI}(\tau)\,\mathrm{d}\tau\right]\\
&+ \mathcal{I}_{LI\to r}(\bar{\varphi})\left[\int_0^t \frac{\partial J^\sigma}{\partial t}\,\dot{N}_{LI}(\tau)\,\mathrm{d}\tau\right]\\
&+ \sum_{i=1}^{4}\left\{\mathcal{I}_{p,i\to r}(\bar{\varphi})\left[\int_0^t \frac{\partial J^\sigma}{\partial t}\,\dot{G}_{p,i}(\tau)\,\mathrm{d}\tau\right]\right\}\\
&+ \sum_{i\in[1,4]}\left\{\mathcal{I}_{s,i\to r}(\bar{\varphi})\left[\int_0^t \frac{\partial J^\sigma}{\partial t}\,\dot{G}_{s,i}(\tau)\,\mathrm{d}\tau\right]\right\},
\end{aligned} \tag{58}$$

while the circumferential components follow the following expression

$$\begin{aligned}
&+\dot{u}_\varphi^M(\bar{\varphi},t) + \dot{u}_r^{\mathrm{MP3}}(t)\sin(\bar{\varphi}) - \dot{u}_\varphi^{\mathrm{MP3}}(t)\cos(\bar{\varphi})\\
&-R\,\dot{\theta}_{z,RI}^M(t)\,\{\cos(\bar{\varphi})-1\}\\
&= \mathcal{I}_{RI\to \varphi}(\bar{\varphi})\left[\int_0^t \frac{\partial J^\sigma}{\partial t}\,\dot{N}_{RI}(\tau)\,\mathrm{d}\tau\right]\\
&+ \mathcal{I}_{LI\to \varphi}(\bar{\varphi})\left[\int_0^t \frac{\partial J^\sigma}{\partial t}\,\dot{N}_{LI}(\tau)\,\mathrm{d}\tau\right]\\
&+ \sum_{i=1}^{4}\left\{\mathcal{I}_{p,i\to \varphi}(\bar{\varphi})\left[\int_0^t \frac{\partial J^\sigma}{\partial t}\,\dot{G}_{p,i}(\tau)\,\mathrm{d}\tau\right]\right\}\\
&+ \sum_{i\in[1,4]}\left\{\mathcal{I}_{s,i\to \varphi}(\bar{\varphi})\left[\int_0^t \frac{\partial J^\sigma}{\partial t}\,\dot{G}_{s,i}(\tau)\,\mathrm{d}\tau\right]\right\},
\end{aligned} \tag{59}$$

and the generator rotation rates obey

$$\begin{aligned}
&+\dot{\theta}_z^M(\bar{\varphi},t) - \dot{\theta}_{z,RI}^M(t)\\
&= \mathcal{I}_{RI\to z}(\bar{\varphi})\left[\int_0^t \frac{\partial J^\sigma}{\partial t}\,\dot{N}_{RI}(\tau)\,\mathrm{d}\tau\right]\\
&+ \mathcal{I}_{LI\to z}(\bar{\varphi})\left[\int_0^t \frac{\partial J^\sigma}{\partial t}\,\dot{N}_{LI}(\tau)\,\mathrm{d}\tau\right]\\
&+ \sum_{i=1}^{4}\left\{\mathcal{I}_{p,i\to z}(\bar{\varphi})\left[\int_0^t \frac{\partial J^\sigma}{\partial t}\,\dot{G}_{p,i}(\tau)\,\mathrm{d}\tau\right]\right\}\\
&+ \sum_{i\in[1,4]}\left\{\mathcal{I}_{s,i\to z}(\bar{\varphi})\left[\int_0^t \frac{\partial J^\sigma}{\partial t}\,\dot{G}_{s,i}(\tau)\,\mathrm{d}\tau\right]\right\}.
\end{aligned} \tag{60}$$

In Eqs. (58) and (59), $\dot{u}_r^M(\bar{\varphi}=0) = \dot{u}_r^{\mathrm{MP3}}$, and $\dot{u}_\varphi^M(\bar{\varphi}=0) = \dot{u}_\varphi^{\mathrm{MP3}}$ denote the displacement rates at the right impost of the shell segment representing the top heading of the Sieberg tunnel, and $\dot{\theta}_z^M(\bar{\varphi}=0) = \dot{\theta}_{z,RI}^M$ denotes the rotation rate at the right impost of the shell segment. Moreover, Eqs. (58)–(60) contain azimuth-dependent influence functions associated with external forces; they are defined through Eqs. (83)–(106) of the Appendix.

6. Solution method for displacement-to-force conversion

In the course of geodetic tunnel monitoring, the displacements at the measurement points MPi, with $i = 1,2,3$, are not available as a continuous function of time t, but measured at discrete points in time t_n, whereby $n = 1,\dots,N_t$, with N_t as the total number of time instants. Consequently, the rates in Eqs. (58)–(60) need to be approximated; and following the procedure outlined by Scharf et al. [17], this is done by assuming linear evolutions of displacements and rotations between the discrete time instants t_{n-1} and t_n, when the displacement measurements were performed. According discretization of the Eqs. (58)–(60), while also considering nonlinear aging power law-type viscoelasticity according to Eqs. (37) and (39), yields

$$\begin{aligned}
&\mathcal{D}_r\big(u_r^M(\bar{\varphi},t_n),\bar{\varphi}\big) = 0 = \frac{u_r^M(\bar{\varphi},t_n) - u_r^M(\bar{\varphi},t_{n-1})}{\Delta t_n}\\
&-\frac{u_r^{\mathrm{MP3}}(t_n) - u_r^{\mathrm{MP3}}(t_{n-1})}{\Delta t_n\,\cos(\bar{\varphi})^{-1}} - \frac{u_\varphi^{\mathrm{MP3}}(t_n) - u_\varphi^{\mathrm{MP3}}(t_{n-1})}{\Delta t_n\,\sin(\bar{\varphi})^{-1}}\\
&+\frac{R\,\theta_{z,RI}^M(t_n) - R\,\theta_{z,RI}^M(t_{n-1})}{\Delta t_n\,\sin(\bar{\varphi})^{-1}}\\
&-\sum_a \mathcal{I}_{a\to r}(\bar{\varphi})\left\{\sum_{m=1}^{N_t}\frac{\eta(t_{n-1})}{E_c\big(\xi(t_n)\big)}\frac{\beta}{t_0^*}\left[\frac{t_n-t_m}{t_0^*}\right]^{\beta-1}\right.\\
&\qquad\left.\times\Big[N_a(t_m) - N_a(t_{m-1})\Big] + \frac{N_a(t_n) - N_a(t_{n-1})}{E\big(\xi(t_n)\big)\Delta t_n}\right\}\\
&-\sum_b \mathcal{I}_{b\to r}(\bar{\varphi})\left\{\sum_{m=1}^{N_t}\frac{\eta(t_{n-1})}{E_c\big(\xi(t_n)\big)}\frac{\beta}{t_0^*}\left[\frac{t_n-t_m}{t_0^*}\right]^{\beta-1}\right.\\
&\qquad\left.\times\Big[G_b(t_m) - G_b(t_{m-1})\Big] + \frac{G_b(t_n) - G_b(t_{n-1})}{E\big(\xi(t_n)\big)\Delta t_n}\right\},
\end{aligned} \tag{61}$$

$$\begin{aligned}
&\mathcal{D}_\varphi\big(u_\varphi^M(\bar{\varphi},t_n),\bar{\varphi}\big) = 0 = \frac{u_\varphi^M(\bar{\varphi},t_n) - u_\varphi^M(\bar{\varphi},t_{n-1})}{\Delta t_n}\\
&+\frac{u_r^{\mathrm{MP3}}(t_n) - u_r^{\mathrm{MP3}}(t_{n-1})}{\Delta t_n\,\sin(\bar{\varphi})^{-1}} - \frac{u_\varphi^{\mathrm{MP3}}(t_n) - u_\varphi^{\mathrm{MP3}}(t_{n-1})}{\Delta t_n\,\cos(\bar{\varphi})^{-1}}\\
&+\frac{R\,\theta_{z,RI}^M(t_n) - R\,\theta_{z,RI}^M(t_{n-1})}{\Delta t_n\big(\cos(\bar{\varphi})-1\big)^{-1}}\\
&-\sum_a \mathcal{I}_{a\to \varphi}(\bar{\varphi})\left\{\sum_{m=1}^{N_t}\frac{\eta(t_{n-1})}{E_c\big(\xi(t_n)\big)}\frac{\beta}{t_0^*}\left[\frac{t_n-t_m}{t_0^*}\right]^{\beta-1}\right.\\
&\qquad\left.\times\Big[N_a(t_m) - N_a(t_{m-1})\Big] + \frac{N_a(t_n) - N_a(t_{n-1})}{E\big(\xi(t_n)\big)\Delta t_n}\right\}\\
&-\sum_b \mathcal{I}_{b\to \varphi}(\bar{\varphi})\left\{\sum_{m=1}^{N_t}\frac{\eta(t_{n-1})}{E_c\big(\xi(t_n)\big)}\frac{\beta}{t_0^*}\left[\frac{t_n-t_m}{t_0^*}\right]^{\beta-1}\right.\\
&\qquad\left.\times\Big[G_b(t_m) - G_b(t_{m-1})\Big] + \frac{G_b(t_n) - G_b(t_{n-1})}{E\big(\xi(t_n)\big)\Delta t_n}\right\},
\end{aligned} \tag{62}$$

$$\begin{aligned}
&\mathcal{D}_z\big(\theta_z^M(\bar{\varphi},t_n),\bar{\varphi}\big) = 0 = \frac{\theta_z^M(t_n) - \theta_z^M(t_{n-1})}{\Delta t_n}\\
&-\frac{\theta_{z,RI}^M(t_n) - \theta_{z,RI}^M(t_{n-1})}{\Delta t_n}\\
&-\sum_a \mathcal{I}_{a\to z}(\bar{\varphi})\left\{\sum_{m=1}^{N_t}\frac{\eta(t_{n-1})}{E_c\big(\xi(t_n)\big)}\frac{\beta}{t_0^*}\left[\frac{t_n-t_m}{t_0^*}\right]^{\beta-1}\right.\\
&\qquad\left.\times\Big[N_a(t_m) - N_a(t_{m-1})\Big] + \frac{N_a(t_n) - N_a(t_{n-1})}{E\big(\xi(t_n)\big)\Delta t_n}\right\}\\
&-\sum_b \mathcal{I}_{b\to z}(\bar{\varphi})\left\{\sum_{m=1}^{N_t}\frac{\eta(t_{n-1})}{E_c\big(\xi(t_n)\big)}\frac{\beta}{t_0^*}\left[\frac{t_n-t_m}{t_0^*}\right]^{\beta-1}\right.\\
&\qquad\left.\times\Big[G_b(t_m) - G_b(t_{m-1})\Big] + \frac{G_b(t_n) - G_b(t_{n-1})}{E\big(\xi(t_n)\big)\Delta t_n}\right\},
\end{aligned} \tag{63}$$

with the time intervals $\Delta t_n = t_n - t_{n-1}$, with $a \in [RI;LI]$, and with $b \in [p,1;p,2;p,3;p,4;s,1;s,4]$.

Together with the three equilibrium conditions of Eqs. (32)–(34) and the shear activation relation of Eq. (14), the external force-to-displacement/rotation conversion relations of Eqs. (61)–(63) provide ten equations for the ten unknowns governing the investigated structural problem. These unknowns need to be determined for every time instant t_n. They are:

$$\begin{aligned}
&G_{p,1}(t_n), G_{p,2}(t_n), G_{p,3}(t_n), G_{p,4}(t_n),\\
&G_{s,1}(t_n), G_{s,4}(t_n), N_{RI}(t_n), N_{LI}(t_n),\\
&\theta_{z,RI}^M(t_n), \theta_{z,LI}^M(t_n).
\end{aligned} \tag{64}$$

The corresponding ten algebraic equations are the following:

- The first three equations have been already given as Eqs. (32)–(34).
- Two equations result from specification of the temporally evolving fields of radial displacements according to Eq. (61), for the corresponding measurements conducted at MP1 and MP2; they read as

$$\mathcal{D}_r\left(u_r^M(\Delta\varphi/2,t_n)=u_r^{\mathrm{MP1}}(t_n),\Delta\varphi/2\right)=0\,, \tag{65}$$

$$\mathcal{D}_r\left(u_r^M(\Delta\varphi,t_n)=u_r^{\mathrm{MP2}}(t_n),\Delta\varphi\right)=0\,, \tag{66}$$

  whereby the histories of the radial displacements of the measurement points MP1 to MP3, i.e. $u_r^{\mathrm{MP1}}(t)$, $u_r^{\mathrm{MP2}}(t)$, $u_r^{\mathrm{MP3}}(t)$, are given in Table 2.
- Two equations result from specification of the temporally evolving fields of tangential displacements according to Eq. (62), for the corresponding measurements conducted at MP1 and MP2; they read as

$$\mathcal{D}_\varphi\left(u_\varphi^M(\Delta\varphi/2,t_n)=u_\varphi^{\mathrm{MP1}}(t_n),\Delta\varphi/2\right)=0\,, \tag{67}$$

$$\mathcal{D}_\varphi\left(u_\varphi^M(\Delta\varphi,t_n)=u_\varphi^{\mathrm{MP2}}(t_n),\Delta\varphi\right)=0\,, \tag{68}$$

  whereby the histories of the tangential displacements of the measurement points MP1 to MP3, i.e. $u_\varphi^{\mathrm{MP1}}(t)$, $u_\varphi^{\mathrm{MP2}}(t)$, $u_\varphi^{\mathrm{MP3}}(t)$, are given in Table 2.
- One equation results from specification of the temporally evolving field of rotation angles according to Eq. (63), for the unknown $\theta_{z,LI}^M(t_n)$; it reads as

$$\mathcal{D}_z\left(\theta_z^M(\Delta\varphi,t_n)=\theta_{z,LI}^M(t_n),\Delta\varphi\right)=0\,. \tag{69}$$

- And two equations result from the connection of the end shear traction forces with the prevailing ground pressure via the so-called proportionality factor $k_{s,p}$,

$$G_{s,i}/G_{p,i}=k_{s,p}\,, \tag{70}$$

  with $i=1,4$. In the present case, the implications of $k_{s,p}\in\{0.00,0.25,0.50,0.75,1.00\}$ are investigated, see also Section 2.

7. Results and discussion

Expectedly, increasing friction activation at the ground–shell interface leads to increasing ground shear forces, compare the subfigures (b_1) and (b_2) of Figs. 5–9. This trend is accompanied by decreasing ground pressures, which, in addition, change from a uniform to a non-uniform spatial distribution, with the maximum magnitude occurring at the crown of the top heading, compare the subfigures (a_1) and (a_2) of Figs. 5–9. The circumferential normal forces follow the same trend as the ground pressures, being reduced with increasing shear transfer from the shell to the ground, with uniform nature at low friction and non-uniform nature at high friction, see the subfigures (c_1) and (c_2) of Figs. 5–9. The opposite trend is seen for the bending moments around the longitudinal direction, which increase with increasing frictional behavior of the soil–ground interface, see the subfigures (d_1) and (d_2) of Figs. 5–9. However, as the mechanical action of the bending moments is subordinate with respect to that of the normal axial forces, the utilization degree follows the trend of the latter, rather than that of the former, i.e. it decreases with increased frictional behavior, see the subfigures (e_1) and (e_2) of Figs. 5–9. As regards the deformational characteristics, increasing friction leads to an increasing number of extrema in the distributions of radial displacements and generator rotations, while the circumferential displacement distributions stay fairly unaffected by the shear transfer at the shell–ground interface, see the subfigures (f_1) and (f_2), (g_1) and (g_2), (h_1) and (h_2) of Figs. 5–9.

Our semi-analytical method also provides novel avenues for the tackling of tunnel design questions, by varying design parameters. As an example we vary the tunnel opening angle $\Delta\varphi$, while keeping the external forces constant, at the levels given through ground pressure and ground shear distributions depicted in Subfigures (a) and (b) of Figs. 5 to 9. In other words, we study the effect of changing the position of the left impost, i.e. of the introduction of some asymmetry in the geometrical characteristics of the top heading cross section, on the distribution of the internal forces. From a mathematical perspective, we consider the normal forces and bending moments as functions of both the circumferential coordinate and the opening angle of the tunnel cross section, i.e. $m_z=m_z(\bar\varphi,\Delta\varphi)$ and $n_\varphi=n_\varphi(\bar\varphi,\Delta\varphi)$, we consider similar functional assignment for the influence functions of Eqs. (73) to (82), and we then derive the Eqs. (30) and (31) with respect to $\Delta\varphi$; this yields

$$\begin{aligned}\frac{\partial n_\varphi(\bar\varphi,\Delta\varphi)}{\partial(\Delta\varphi)} &= N_{RI}\,\frac{\partial \mathcal{I}_{RI\to f}(\bar\varphi,\Delta\varphi)}{\partial(\Delta\varphi)}\\ &+ N_{LI}\,\frac{\partial \mathcal{I}_{LI\to f}(\bar\varphi,\Delta\varphi)}{\partial(\Delta\varphi)}\\ &+ \textstyle\sum_{i=1}^{4} R\,G_{p,i}\,\frac{\partial \mathcal{I}_{p,i\to f}(\bar\varphi,\Delta\varphi)}{\partial(\Delta\varphi)}\\ &+ \textstyle\sum_{i\in[1,4]}\left[R-\frac{h}{2}\right]G_{s,i}\,\frac{\partial \mathcal{I}_{s,i\to f}(\bar\varphi,\Delta\varphi)}{\partial(\Delta\varphi)}\,,\end{aligned} \tag{71}$$

and

$$\begin{aligned}\frac{\partial m_z(\bar\varphi,\Delta\varphi)}{\partial(\Delta\varphi)} &= -R\,N_{RI}\,\frac{\partial \mathcal{I}_{RI\to f}(\bar\varphi,\Delta\varphi)}{\partial(\Delta\varphi)}\\ &- R\,N_{LI}\,\frac{\partial \mathcal{I}_{LI\to f}(\bar\varphi,\Delta\varphi)}{\partial(\Delta\varphi)}\\ &+ \textstyle\sum_{i=1}^{4} R^2\,G_{p,i}\,\frac{\partial \mathcal{I}_{p,i\to f}(\bar\varphi,\Delta\varphi)}{\partial(\Delta\varphi)}\\ &- \textstyle\sum_{i\in[1,4]}\left[R^2\right]G_{s,i}\,\frac{\partial \mathcal{I}_{s,i\to m}(\bar\varphi,\Delta\varphi)}{\partial(\Delta\varphi)}\\ &- \textstyle\sum_{i\in[1,4]}\left[R^2-\frac{R\,h}{2}\right]G_{s,i}\,\frac{\partial \mathcal{I}_{s,i\to f}(\bar\varphi,\Delta\varphi)}{\partial(\Delta\varphi)}\,,\end{aligned} \tag{72}$$

whereby the partial derivatives of the influence functions are given through Eqs. (119)–(128) of the Appendix. As major result of this design study, it is observed that, in case of significant ground–shell traction transfer, an increase of the opening angle, i.e. setting the left impost downward, results in a general increase of the magnitude of the normal force, see Fig. 10(b), together with a decrease of the moment magnitude at the tunnel crown, accompanied by an increase of the moment magnitude laterally, see Fig. 10(a). Hence, introduction of asymmetry does not appear as beneficial design feature, since increasing compression with mixed bending effects will generally increase the utilization degree. Still, asymmetry-inducing infinitesimal change of the tunnel geometry has no effect on the internal force distribution, as long as the ground–shell traction transfer remains negligible.

It is interesting to set our approach in context to the wide field of structural mechanics applied to tunnel engineering [82–84]. As a first key characteristic, we note that our approach does neither compare the predictions of a computational model of the tunnel shell and the surrounding ground to field data, nor does it encompass corresponding quantitative validation procedures with statistical elements. Our approach rather constitutes an important complement to such more customary studies, by directly integrating available field data, i.e. geodetic displacement measurements in the present case, into a structural mechanics analysis. It hence qualifies as what has been coined as “hybrid methods” [10,11], with applications in traditional NATM-tunneling [85], in segmented NATM-tunnels driven in squeezing rock [13], as well as in mechanized tunnel engineering [86]. With respect to conventional approaches where a uniform ground pressure [87] or very specific ground pressure distributions, such as a “pure shear configuration” [88], are introduced, the present approach sets the very emphasis on the ground shear action as function of the behavior of the interface between ground and tunnel shell. Customarily, this phenomenon is ignored, and only the limit cases, referring to perfect contact between shell and ground (relating to infinite shear transmission capacity of the ground–shell interface) as well as to “full slip” between shell and ground (relating to zero transmission capacity of the ground–shell interface), are considered [87]. Hence, our approach delivers unprecedented insight into the fundamental

load-carrying characteristic of an NATM tunnel, elucidating, even qualitatively, the functioning of such shells, up to a level of understanding which has not been attained so far. Accordingly, there are very few published reports which allow some type of "more direct comparison" with our new approach. These reports concern simulations based on the distinct element method (DEM), of tunnel–ground systems with explicit modeling of the shell-to-ground interface [88,89]: The DEM report [88] on bending moments increasing with increased irregularity, and hence with increased shear activation, of the shell–ground interface, is fully consistent with our herein reported increase of bending moments with increasing shear force transmission, as seen from the Subfigures (d) of Figs. 5 to 9. However, the aforementioned DEM study does not include any field data, while our study contains field data as a very important, central ingredient. This may explain some discrepancies between the results of the DEM study versus the hybrid analysis presented herein. In more detail, the DEM study leads to increased normal forces, while our study shows overall load decrease and utilization reduction of the tunnel shell, as a consequence of increased friction between shell and ground, see the Subfigures (c) and (e) of Figs. 5 to 9. The reason for the overestimation of normal forces in the DEM simulation reported in [88] may stem from the total neglect of dissipative phenomena, such as elasto-plastic events, in both the ground and the tunnel shell. This conjecture is well supported by yet another suite of DEM simulations, where the shotcrete shell and the rock mass were indeed allowed to behave elasto-plastically [89]. There, increased roughness of the shell-to-ground interface, implying a higher shear transmission capacity, resulted in reduced normal forces in the tunnel shell. This is fully consistent with the results of our field data-driven hybrid analysis, see the Subfigures (c) of Figs. 5 to 9.

Our analysis exhibits several limitations, simplifications, and assumptions:

From a shell theoretical perspective, it is restricted to thin cylindrical shells with constant thickness. While thin cylindrical shells are relevant for the majority of realized NATM projects, the issue of constant thickness, and corresponding deviations from this assumptions due to heavy irregularities of the shell–ground interface could be the topic of interesting investigations. This would require a fundamental re-consideration of the mathematical structure of shell-specific internal forces, as the key normal stresses would not act any more in directions parallel to the tangent plane of the shell midsurface. Such developments, which may be based on the concepts set forth in [90–93] are clearly beyond the scope of the present manuscript.

From a construction process engineering viewpoint, our study is restricted to the first construction step in a sequential tunnel excavation scheme, that related to the excavation and installation of the top heading of the tunnel. Extension to the entire excavation procedure would require the formulation of dedicated displacement and force transfer conditions between the top heading and the benches, on the one hand, and between the benches and the invert, on the other hand. Earlier, fully geometrically driven versions of hybrid methods for shotcrete tunnel safety assessment [11,94] have provided such transfer conditions for the displacements. In the current conceptual context, transfer relations [95] for both forces and displacements would be required; and at the same time, the theoretical implications of a non-constant radius of the shell midsurface would need to be understood. While this is beyond the scope of the present manuscript, it is a topic of strong current interest.

Moreover, the limited number of measurement points, realized in terms of three geodetic reflectors installed along the circumference of the top heading of the tunnel, implies simplifications and assumptions concerning the distributions of the external forces acting from the ground onto the tunnel shell: Ground force values are determined at four locations and cubic polynomials are employed for interpolation in between. In case more measurement points are realized, such as with tunnel Stein [96], ground force values can be determined at more than four, e.g. eight, locations along the tunnel circumference [85]. Hence, the concept applied here to the Sieberg tunnel, characterized by three measurement points, can be adapted to other tunnel design settings. However, the choice of appropriate interpolation functions and the realization of a corresponding solution method need careful reflection and development.

Concerning the interpolation scheme for ground action, another note is due: Ground shear forces are only introduced near the imposts and not at the tunnel crown. This can be physically motivated by shear forces arising from relative motions between the ground and the tunnel shell, and by these motions, in turn, being mainly driven through vertically acting gravitational forces. In addition, this choice of shear force patterns is consistent with results stemming from displacement interpolation combined with shell kinematics and local equilibrium conditions from 3D continuum mechanics [14], which, in turn, are consistent with classical rock load estimates of Terzaghi [97].

8. Conclusion

A novel analytical structural mechanics model for a top heading of an NATM tunnel, which considers not only ground pressure, but also ground shear forces acting, from the surrounding ground, onto the tunnel shell, allows for the following, interesting conclusion: On top of the well-known ground strengthening through rock bolts, which saves an NATM tunnel shell from being exceedingly loaded by forces arising from the configurational changes due to the tunnel excavation process along with the creep behavior of both soil and shotcrete, it is the shear transfer at the shell-to-rock interface, which additionally spares the shell from excessive mechanical utilization.

CRediT authorship contribution statement

Raphael Scharf: Writing – original draft, Visualization, Validation, Software, Investigation, Formal analysis. **Christian Hellmich:** Writing – review & editing, Writing – original draft, Supervision, Methodology, Funding acquisition, Conceptualization.

Declaration of competing interest

The authors declare that they have no known competing financial interests or personal relationships that could have appeared to influence the work reported in this paper.

Acknowledgments

The authors gratefully acknowledge project FFG-COMET #882504 "Rail4Future: Resilient Digital Railway Systems to enhance performance". They also acknowledge TU Wien Bibliothek for financial support through its Open Access Funding Programme.

Appendix. Azimuth-dependent influence functions

Eqs. (30) and (31), which link the external forces to the internal forces, include the following influence functions,

$$\mathcal{I}_{RI\to f}(\bar{\varphi}) = \cos(\bar{\varphi}) - \frac{\sin(\bar{\varphi})}{\tan(\Delta\varphi)}\,, \tag{73}$$

$$\mathcal{I}_{LI\to f}(\bar{\varphi}) = \frac{\sin(\bar{\varphi})}{\cos(\Delta\varphi)}\,, \tag{74}$$

$$\begin{aligned}\mathcal{I}_{p,1\to f}(\bar{\varphi}) = {} & 1 + \frac{27\bar{\varphi}}{\Delta\varphi^3} - \frac{9\bar{\varphi}^3}{2\Delta\varphi^3} \\ & - \frac{18}{\Delta\varphi^2} + \frac{9\bar{\varphi}^2}{\Delta\varphi^2} - \frac{11\bar{\varphi}}{2\Delta\varphi} \\ & - \cos(\bar{\varphi}) + \frac{18\cos(\bar{\varphi})}{\Delta\varphi^2} + \frac{\sin(\bar{\varphi})}{\tan(\Delta\varphi)} \\ & - \frac{18\sin(\bar{\varphi})}{\Delta\varphi^2\tan(\Delta\varphi)} - \frac{9\sin(\bar{\varphi})}{\Delta\varphi^2\sin(\Delta\varphi)}\,,\end{aligned} \tag{75}$$

$$\mathcal{I}_{p,2\to f}(\bar{\varphi}) = -\frac{81\bar{\varphi}}{\Delta\varphi^3} + \frac{27\bar{\varphi}^3}{2\Delta\varphi^3} + \frac{45}{\Delta\varphi^2} - \frac{45\bar{\varphi}^2}{2\Delta\varphi^2} + \frac{9\bar{\varphi}}{\Delta\varphi} - \frac{45\cos(\bar{\varphi})}{\Delta\varphi^2} + \frac{45\sin(\bar{\varphi})}{\Delta\varphi^2\tan(\Delta\varphi)} + \frac{36\sin(\Delta\varphi)\sin(\bar{\varphi})}{\Delta\varphi^2\sin(\Delta\varphi)}, \tag{76}$$

$$\mathcal{I}_{p,3\to f}(\bar{\varphi}) = \frac{81\bar{\varphi}}{\Delta\varphi^3} - \frac{27\bar{\varphi}^3}{2\Delta\varphi^3} - \frac{36}{\Delta\varphi^2} + \frac{18\bar{\varphi}^2}{\Delta\varphi^2} - \frac{9\bar{\varphi}}{2\Delta\varphi} + \frac{36\cos(\bar{\varphi})}{\Delta\varphi^2} - \frac{36\sin(\bar{\varphi})}{\Delta\varphi^2\tan(\Delta\varphi)} - \frac{45\sin(\bar{\varphi})}{\Delta\varphi^2\sin(\Delta\varphi)}, \tag{77}$$

$$\mathcal{I}_{p,4\to f}(\bar{\varphi}) = -\frac{27\bar{\varphi}}{\Delta\varphi^3} + \frac{9\bar{\varphi}^3}{2\Delta\varphi^3} + \frac{9}{\Delta\varphi^2} - \frac{9\bar{\varphi}^2}{2\Delta\varphi^2} + \frac{\bar{\varphi}}{\Delta\varphi} - \frac{9\cos(\bar{\varphi})}{\Delta\varphi^2} + \frac{9\sin(\bar{\varphi})}{\Delta\varphi^2\tan(\Delta\varphi)} - \frac{\sin(\bar{\varphi})}{\sin(\Delta\varphi)} + \frac{18\sin(\bar{\varphi})}{\Delta\varphi^2\sin(\Delta\varphi)}, \tag{78}$$

$$\mathcal{I}_{s,1\to m}(\bar{\varphi}) = -\bar{\varphi} + \frac{9\bar{\varphi}^4}{8\Delta\varphi^3} - \frac{3\bar{\varphi}^3}{\Delta\varphi^2} + \frac{11\bar{\varphi}^2}{4\Delta\varphi}, \tag{79}$$

$$\mathcal{I}_{s,4\to m}(\bar{\varphi}) = \frac{3\bar{\varphi}^3}{2\Delta\varphi^2} - \frac{\bar{\varphi}^2}{2\Delta\varphi}, \tag{80}$$

$$\mathcal{I}_{s,1\to f}(\bar{\varphi}) = \frac{27\bar{\varphi}^2}{2\Delta\varphi^3} - \frac{27}{\Delta\varphi^3} + \frac{11}{2\Delta\varphi} - \frac{18\bar{\varphi}}{\Delta\varphi^2} + \frac{27\cos(\bar{\varphi})}{\Delta\varphi^3} - \frac{11\cos(\bar{\varphi})}{2\Delta\varphi} - \frac{27\sin(\bar{\varphi})}{\Delta\varphi^3\tan(\Delta\varphi)} + \frac{11\sin(\bar{\varphi})}{2\Delta\varphi\tan(\Delta\varphi)} + \frac{27\sin(\bar{\varphi})}{\Delta\varphi^3\sin(\Delta\varphi)} - \frac{\sin(\bar{\varphi})}{\Delta\varphi\sin(\Delta\varphi)}, \tag{81}$$

$$\mathcal{I}_{s,4\to f}(\bar{\varphi}) = -\frac{27\bar{\varphi}^2}{2\Delta\varphi^3} + \frac{9\bar{\varphi}}{\Delta\varphi^2} - \frac{1}{\Delta\varphi} - \frac{27\cos(\bar{\varphi})}{\Delta\varphi^3} + \frac{\cos(\bar{\varphi})}{\Delta\varphi} - \frac{\sin(\bar{\varphi})}{\Delta\varphi\tan(\Delta\varphi)} - \frac{27\sin(\bar{\varphi})}{\Delta\varphi^3\sin(\Delta\varphi)} + \frac{11\sin(\bar{\varphi})}{2\Delta\varphi\sin(\Delta\varphi)}. \tag{82}$$

Eqs. (58) and (61), which link the rates of the external forces to the rates of the radial displacements, include the following influence functions,

$$\mathcal{I}_{RI\to r}(\bar{\varphi}) = \left\{1-\nu^2\right\}\left\{\frac{12R^3}{h^3}\left[\cos(\bar{\varphi})-1\right] + \left[\frac{R}{2h}+\frac{6R^3}{h^3}\right]\left[\frac{\bar{\varphi}\cos(\bar{\varphi})}{\tan(\Delta\varphi)} + \bar{\varphi}\sin(\bar{\varphi}) - \frac{\sin(\bar{\varphi})}{\tan(\Delta\varphi)}\right]\right\}, \tag{83}$$

$$\mathcal{I}_{LI\to r}(\bar{\varphi}) = \left\{1-\nu^2\right\}\left\{\left[\frac{R}{2h}+\frac{6R^3}{h^3}\right]\left[\frac{\sin(\bar{\varphi})}{\sin(\Delta\varphi)} - \frac{\bar{\varphi}\cos(\bar{\varphi})}{\sin(\Delta\varphi)}\right]\right\}, \tag{84}$$

$$\mathcal{I}_{p,1\to r}(\bar{\varphi}) = \left\{1-\nu^2\right\}\left\{\left[\frac{R^2}{h}+\frac{12R^4}{h^3}\right]\left[-1 - \frac{54\bar{\varphi}}{(\Delta\varphi)^3} + \frac{9\bar{\varphi}^3}{2(\Delta\varphi)^3} + \frac{36}{(\Delta\varphi)^2} - \frac{9\bar{\varphi}^2}{(\Delta\varphi)^2} + \frac{11\bar{\varphi}}{2\Delta\varphi} - \frac{36\cos(\bar{\varphi})}{(\Delta\varphi)^2} + \frac{\bar{\varphi}\cos(\bar{\varphi})}{2\tan(\Delta\varphi)} - \frac{9\bar{\varphi}\cos(\bar{\varphi})}{(\Delta\varphi)^2\tan(\Delta\varphi)} + \cos(\bar{\varphi}) - \frac{9\bar{\varphi}\cos(\bar{\varphi})}{2(\Delta\varphi)^2\sin(\Delta\varphi)} + \frac{\bar{\varphi}\sin(\bar{\varphi})}{2} + \frac{54\sin(\bar{\varphi})}{(\Delta\varphi)^3} - \frac{9\bar{\varphi}\sin(\bar{\varphi})}{(\Delta\varphi)^2} - \frac{11\sin(\bar{\varphi})}{2\Delta\varphi} - \frac{\sin(\bar{\varphi})}{2\tan(\Delta\varphi)} + \frac{9\sin(\bar{\varphi})}{(\Delta\varphi)^2\tan(\Delta\varphi)} + \frac{9\sin(\bar{\varphi})}{2(\Delta\varphi)^2\sin(\Delta\varphi)}\right]\right\}, \tag{85}$$

$$\mathcal{I}_{p,2\to r}(\bar{\varphi}) = \left\{1-\nu^2\right\}\left\{\left[\frac{R^2}{h}+\frac{12R^4}{h^3}\right]\left[\frac{162\bar{\varphi}}{(\Delta\varphi)^3} - \frac{27\bar{\varphi}^3}{2(\Delta\varphi)^3} - \frac{90}{(\Delta\varphi)^2} + \frac{45\bar{\varphi}^2}{2(\Delta\varphi)^2} - \frac{9\bar{\varphi}}{\Delta\varphi} + \frac{90\cos(\bar{\varphi})}{(\Delta\varphi)^2} + \frac{45\bar{\varphi}\cos(\bar{\varphi})}{2(\Delta\varphi)^2\tan(\Delta\varphi)} + \frac{18\bar{\varphi}\cos(\bar{\varphi})}{(\Delta\varphi)^2\sin(\Delta\varphi)} - \frac{162\sin(\bar{\varphi})}{(\Delta\varphi)^3} + \frac{45\bar{\varphi}\sin(\bar{\varphi})}{2(\Delta\varphi)^2} - \frac{45\sin(\bar{\varphi})}{2(\Delta\varphi)^2\tan(\Delta\varphi)} + \frac{9\sin(\bar{\varphi})}{\Delta\varphi} - \frac{18\sin(\bar{\varphi})}{(\Delta\varphi)^2\sin(\Delta\varphi)}\right]\right\}, \tag{86}$$

$$\mathcal{I}_{p,3\to r}(\bar{\varphi}) = \left\{1-\nu^2\right\}\left\{\left[\frac{R^2}{h}+\frac{12R^4}{h^3}\right]\left[-\frac{162\bar{\varphi}}{(\Delta\varphi)^3} + \frac{27\bar{\varphi}^3}{2(\Delta\varphi)^3} + \frac{72}{(\Delta\varphi)^2} - \frac{18\bar{\varphi}^2}{(\Delta\varphi)^2} + \frac{9\bar{\varphi}}{2\Delta\varphi} - \frac{72\cos(\bar{\varphi})}{(\Delta\varphi)^2} - \frac{18\bar{\varphi}\cos(\bar{\varphi})}{(\Delta\varphi)^2\tan(\Delta\varphi)} - \frac{45\bar{\varphi}\cos(\bar{\varphi})}{2(\Delta\varphi)^2\sin(\Delta\varphi)} + \frac{162\sin(\bar{\varphi})}{(\Delta\varphi)^3} - \frac{18\bar{\varphi}\sin(\bar{\varphi})}{(\Delta\varphi)^2} + \frac{18\sin(\bar{\varphi})}{(\Delta\varphi)^2\tan(\Delta\varphi)} - \frac{9\sin(\bar{\varphi})}{2\Delta\varphi} + \frac{45\sin(\bar{\varphi})}{2(\Delta\varphi)^2\sin(\Delta\varphi)}\right]\right\}, \tag{87}$$

$$\mathcal{I}_{p,4\to r}(\bar{\varphi}) = \left\{1-\nu^2\right\}\left\{\left[\frac{R^2}{h}+\frac{12R^4}{h^3}\right]\left[\frac{54\bar{\varphi}}{(\Delta\varphi)^3} - \frac{9\bar{\varphi}^3}{2(\Delta\varphi)^3} - \frac{18}{(\Delta\varphi)^2} + \frac{9\bar{\varphi}^2}{2(\Delta\varphi)^2} - \frac{\bar{\varphi}}{\Delta\varphi} + \frac{18\cos(\bar{\varphi})}{(\Delta\varphi)^2} + \frac{9\bar{\varphi}\cos(\bar{\varphi})}{2(\Delta\varphi)^2\tan(\Delta\varphi)} - \frac{54\sin(\bar{\varphi})}{(\Delta\varphi)^3} + \frac{9\bar{\varphi}\cos(\bar{\varphi})}{(\Delta\varphi)^2\sin(\Delta\varphi)} + \frac{9\bar{\varphi}\sin(\bar{\varphi})}{2(\Delta\varphi)^2} - \frac{\bar{\varphi}\cos(\bar{\varphi})}{2\sin(\Delta\varphi)} + \frac{\sin(\bar{\varphi})}{\Delta\varphi} - \frac{9\sin(\bar{\varphi})}{2(\Delta\varphi)^2\tan(\Delta\varphi)} + \frac{\sin(\bar{\varphi})}{2\sin(\Delta\varphi)} - \frac{9\sin(\bar{\varphi})}{(\Delta\varphi)^2\sin(\Delta\varphi)}\right]\right\}, \tag{88}$$

$$
\begin{aligned}
\mathcal{I}_{s,1\to r}(\bar{\varphi}) = & \left\{1-\nu^2\right\}\left\{\left[\frac{R^2}{h}-\frac{R}{2}-\frac{12R^3}{h^2}\right]\right. \\
& \times\left[\frac{54\cos(\bar{\varphi})-54}{(\Delta\varphi)^3}\right]+\frac{12R^4}{h^3}\left[\bar{\varphi}\right. \\
& -\frac{81}{(\Delta\varphi)^3}-\frac{9\bar{\varphi}^4}{8(\Delta\varphi)^3}+\frac{3\bar{\varphi}^3}{(\Delta\varphi)^2}-\frac{11\bar{\varphi}^2}{4\Delta\varphi} \\
& +\frac{81\cos(\bar{\varphi})}{(\Delta\varphi)^3}-\sin(\bar{\varphi})\left.\right]+\left[\frac{R^2}{h}-\frac{R}{2}\right. \\
& -\frac{6R^3}{h^2}+\frac{12R^4}{h^3}\left.\right]\left[\frac{27\bar{\varphi}\cos(\bar{\varphi})}{2(\Delta\varphi)^3\tan(\Delta\varphi)}\right. \\
& -\frac{11\bar{\varphi}\cos(\bar{\varphi})}{4\Delta\varphi\tan(\Delta\varphi)}-\frac{27\bar{\varphi}\cos(\bar{\varphi})}{2(\Delta\varphi)^3\sin(\Delta\varphi)} \\
& +\frac{\bar{\varphi}\cos(\bar{\varphi})}{2\Delta\varphi\sin(\Delta\varphi)}-\frac{27\sin(\bar{\varphi})}{2(\Delta\varphi)^3\tan(\Delta\varphi)} \\
& +\frac{11\sin(\bar{\varphi})}{4\Delta\varphi\tan(\Delta\varphi)}+\frac{27\sin(\bar{\varphi})}{2(\Delta\varphi)^3\sin(\Delta\varphi)} \\
& -\frac{\sin(\bar{\varphi})}{2\Delta\varphi\sin(\Delta\varphi)}+\frac{27\bar{\varphi}\sin(\bar{\varphi})}{2(\Delta\varphi)^3}\left.\right]+\left[\frac{R^2}{h}\right. \\
& -\frac{R}{2}-\frac{6R^3}{h^2}+\frac{24R^4}{h^3}\left.\right]\left[\frac{27\bar{\varphi}^2}{2(\Delta\varphi)^3}\right. \\
& -\frac{18\bar{\varphi}}{(\Delta\varphi)^2}+\frac{11}{2\Delta\varphi}-\frac{11\cos(\bar{\varphi})}{2\Delta\varphi} \\
& +\frac{18\sin(\bar{\varphi})}{(\Delta\varphi)^2}-\frac{11\bar{\varphi}\sin(\bar{\varphi})}{4\Delta\varphi}\left.\right]\Bigg\},
\end{aligned}
\tag{89}
$$

$$
\begin{aligned}
\mathcal{I}_{s,4\to r}(\bar{\varphi}) = & \left\{1-\nu^2\right\}\left\{\left[\frac{R^2}{h}-\frac{R}{2}-\frac{6R^3}{h^2}\right]\right. \\
& \times\left[\frac{54-54\cos(\bar{\varphi})}{(\Delta\varphi)^3}\right]+\frac{12R^4}{h^3}\left[\frac{81}{(\Delta\varphi)^3}\right. \\
& +\frac{9\bar{\varphi}^4}{8(\Delta\varphi)^3}-\frac{3\bar{\varphi}^3}{2(\Delta\varphi)^2}+\frac{\bar{\varphi}^2}{2\Delta\varphi} \\
& -\frac{81\cos(\bar{\varphi})}{(\Delta\varphi)^3}\left.\right]+\left[\frac{R^2}{h}-\frac{R}{2}-\frac{6R^3}{h^2}\right. \\
& +\frac{12R^4}{h^3}\left.\right]\left[-\frac{27\bar{\varphi}\cos(\bar{\varphi})}{2(\Delta\varphi)^3\tan(\Delta\varphi)}\right. \\
& +\frac{\bar{\varphi}\cos(\bar{\varphi})}{2\Delta\varphi\tan(\Delta\varphi)}+\frac{27\bar{\varphi}\cos(\bar{\varphi})}{2(\Delta\varphi)^3\sin(\Delta\varphi)} \\
& -\frac{11\bar{\varphi}\cos(\bar{\varphi})}{4\Delta\varphi\sin(\Delta\varphi)}+\frac{\bar{\varphi}\sin(\bar{\varphi})}{2\Delta\varphi} \\
& -\frac{27\bar{\varphi}\sin(\bar{\varphi})}{2(\Delta\varphi)^3}+\frac{27\sin(\bar{\varphi})}{2(\Delta\varphi)^3\tan(\Delta\varphi)} \\
& -\frac{\sin(\bar{\varphi})}{2\Delta\varphi\tan(\Delta\varphi)}-\frac{27\sin(\bar{\varphi})}{2(\Delta\varphi)^3\sin(\Delta\varphi)} \\
& +\frac{11\sin(\bar{\varphi})}{4\Delta\varphi\sin(\Delta\varphi)}\left.\right]+\left[\frac{R^2}{h}-\frac{R}{2}-\frac{6R^3}{h^2}\right. \\
& +\frac{24R^4}{h^3}\left.\right]\left[-\frac{27\bar{\varphi}^2}{2(\Delta\varphi)^3}+\frac{9\bar{\varphi}}{(\Delta\varphi)^2}\right. \\
& -\frac{1}{\Delta\varphi}+\frac{\cos(\bar{\varphi})}{\Delta\varphi}-\frac{9\sin(\bar{\varphi})}{(\Delta\varphi)^2}\left.\right]\Bigg\}.
\end{aligned}
\tag{90}
$$

Eqs. (59) and (62), which link the rates of the external forces to the rates of the tangential displacements, include the following influence functions,

$$
\begin{aligned}
\mathcal{I}_{RI\to\varphi}(\bar{\varphi}) = & \left\{1-\nu^2\right\}\left\{\left[\frac{R}{2h}+\frac{6R^3}{h^3}\right]\left[\bar{\varphi}\cos(\bar{\varphi})\right.\right. \\
& -3\sin(\bar{\varphi})-\frac{\bar{\varphi}\sin(\bar{\varphi})}{\tan(\Delta\varphi)}\left.\right]+\frac{R}{h}\left[2\sin(\bar{\varphi})\right] \\
& +\frac{12R^3}{h^3}\left[\bar{\varphi}-\frac{\cos(\bar{\varphi})-1}{\tan(\Delta\varphi)}\right]\Bigg\},
\end{aligned}
\tag{91}
$$

$$
\begin{aligned}
\mathcal{I}_{LI\to\varphi}(\bar{\varphi}) = & \left\{1-\nu^2\right\}\left\{\frac{12R^3}{h^3}\left[\frac{\cos(\bar{\varphi})-1}{\sin(\Delta\varphi)}\right]\right. \\
& +\left.\left[\frac{R}{2h}+\frac{6R^3}{h^3}\right]\left[\frac{\bar{\varphi}\sin(\bar{\varphi})}{\sin(\Delta\varphi)}\right]\right\},
\end{aligned}
\tag{92}
$$

$$
\begin{aligned}
\mathcal{I}_{p,1\to\varphi}(\bar{\varphi}) = & \left\{1-\nu^2\right\}\left\{\left[\frac{R^2}{h}+\frac{12R^4}{h^3}\right]\right. \\
& \times\left[\frac{11-11\cos(\bar{\varphi})}{2\Delta\varphi}-\frac{54-54\cos(\bar{\varphi})}{(\Delta\varphi)^3}\right. \\
& +\frac{\bar{\varphi}\cos(\bar{\varphi})}{2}-\frac{9\bar{\varphi}\cos(\bar{\varphi})}{(\Delta\varphi)^2}-\frac{\bar{\varphi}\sin(\bar{\varphi})}{2\tan(\Delta\varphi)} \\
& +\frac{9\bar{\varphi}\sin(\bar{\varphi})}{(\Delta\varphi)^2\tan(\Delta\varphi)}+\frac{9\bar{\varphi}\sin(\bar{\varphi})}{2(\Delta\varphi)^2\sin(\Delta\varphi)}\left.\right] \\
& +\frac{R^2}{h}\left[+\frac{27\bar{\varphi}^2}{2(\Delta\varphi)^3}-\frac{18\bar{\varphi}}{(\Delta\varphi)^2}-\frac{\sin(\bar{\varphi})}{2}\right. \\
& +\frac{27\sin(\bar{\varphi})}{(\Delta\varphi)^2}\left.\right]+\frac{12R^4}{h^3}\left[\bar{\varphi}+\frac{3\bar{\varphi}^3}{(\Delta\varphi)^2}\right. \\
& -\frac{9\bar{\varphi}^4}{8(\Delta\varphi)^3}-\frac{11\bar{\varphi}^2}{4\Delta\varphi}+\frac{27\bar{\varphi}^2}{(\Delta\varphi)^3}-\frac{36\bar{\varphi}}{(\Delta\varphi)^2} \\
& -\frac{3\sin(\bar{\varphi})}{2}+\frac{45\sin(\bar{\varphi})}{(\Delta\varphi)^2}+\frac{1-\cos(\bar{\varphi})}{\tan(\Delta\varphi)} \\
& -\left.\frac{9-9\cos(\bar{\varphi})}{(\Delta\varphi)^2\sin(\Delta\varphi)}-\frac{18-18\cos(\bar{\varphi})}{(\Delta\varphi)^2\tan(\Delta\varphi)}\right]\Bigg\},
\end{aligned}
\tag{93}
$$

$$
\begin{aligned}
\mathcal{I}_{p,2\to\varphi}(\bar{\varphi}) = & \left\{1-\nu^2\right\}\left\{\left[\frac{R^2}{h}+\frac{12R^4}{h^3}\right]\right. \\
& \times\left[\frac{162-162\cos(\bar{\varphi})}{(\Delta\varphi)^3}-\frac{9-9\cos(\bar{\varphi})}{\Delta\varphi}\right. \\
& -\frac{45\bar{\varphi}\sin(\bar{\varphi})}{2(\Delta\varphi)^2\tan(\Delta\varphi)}-\frac{18\bar{\varphi}\sin(\bar{\varphi})}{(\Delta\varphi)^2\sin(\Delta\varphi)} \\
& +\frac{45\bar{\varphi}\cos(\bar{\varphi})}{2(\Delta\varphi)^2}\left.\right]+\frac{12R^4}{h^3}\left[-\frac{81\bar{\varphi}^2}{(\Delta\varphi)^3}\right. \\
& +\frac{27\bar{\varphi}^4}{8(\Delta\varphi)^3}+\frac{90\bar{\varphi}}{(\Delta\varphi)^2}-\frac{15\bar{\varphi}^3}{2(\Delta\varphi)^2}+\frac{9\bar{\varphi}^2}{2\Delta\varphi} \\
& +\frac{45-45\cos(\bar{\varphi})}{(\Delta\varphi)^2\tan(\Delta\varphi)}+\frac{36-36\cos(\bar{\varphi})}{(\Delta\varphi)^2\sin(\Delta\varphi)} \\
& -\frac{225\sin(\bar{\varphi})}{2(\Delta\varphi)^2}\left.\right]+\frac{R^2}{h}\left[-\frac{81\bar{\varphi}^2}{2(\Delta\varphi)^3}\right. \\
& +\left.\frac{45\bar{\varphi}}{(\Delta\varphi)^2}-\frac{135\sin(\bar{\varphi})}{2(\Delta\varphi)^2}\right]\Bigg\},
\end{aligned}
\tag{94}
$$

$$
\begin{aligned}
\mathcal{I}_{p,3\to\varphi}(\bar{\varphi}) = & \left\{1-\nu^2\right\}\left\{\left[\frac{R^2}{h}+\frac{12R^4}{h^3}\right]\right. \\
& \times\left[-\frac{162-162\cos(\bar{\varphi})}{(\Delta\varphi)^3}+\frac{9-9\cos(\bar{\varphi})}{2\Delta\varphi}\right. \\
& -\frac{18\bar{\varphi}\cos(\bar{\varphi})}{(\Delta\varphi)^2}+\frac{18\bar{\varphi}\sin(\bar{\varphi})}{(\Delta\varphi)^2\tan(\Delta\varphi)} \\
& +\frac{45\bar{\varphi}\sin(\bar{\varphi})}{2(\Delta\varphi)^2\sin(\Delta\varphi)}\left.\right]+\frac{12R^4}{h^3}\left[\frac{81\bar{\varphi}^2}{(\Delta\varphi)^3}\right. \\
& -\frac{27\bar{\varphi}^4}{8(\Delta\varphi)^3}-\frac{72\bar{\varphi}}{(\Delta\varphi)^2}+\frac{6\bar{\varphi}^3}{(\Delta\varphi)^2}-\frac{9\bar{\varphi}^2}{4\Delta\varphi} \\
& -\frac{36-36\cos(\bar{\varphi})}{(\Delta\varphi)^2\tan(\Delta\varphi)}-\frac{45-45\cos(\bar{\varphi})}{(\Delta\varphi)^2\sin(\Delta\varphi)} \\
& +\frac{90\sin(\bar{\varphi})}{(\Delta\varphi)^2}\left.\right]+\frac{R^2}{h}\left[\frac{81\bar{\varphi}^2}{2(\Delta\varphi)^3}-\frac{36\bar{\varphi}}{(\Delta\varphi)^2}\right. \\
& +\left.\frac{54\sin(\bar{\varphi})}{(\Delta\varphi)^2}\right]\Bigg\},
\end{aligned}
\tag{95}
$$

$$
\begin{aligned}
\mathcal{I}_{p,4\to\varphi}(\bar{\varphi}) = & \left\{1-\nu^2\right\}\left\{\left[\frac{R^2}{h}+\frac{12R^4}{h^3}\right]\left[-\frac{1}{\Delta\varphi}\right.\right. \\
& + \frac{54-54\cos(\bar{\varphi})}{\Delta\varphi^3}+\frac{9\bar{\varphi}\cos(\bar{\varphi})}{2\Delta\varphi^2} \\
& - \frac{9\bar{\varphi}\sin(\bar{\varphi})}{2\Delta\varphi^2\tan(\Delta\varphi)}+\frac{\bar{\varphi}\sin(\bar{\varphi})}{2\sin(\Delta\varphi)} \\
& \left. - \frac{9\bar{\varphi}\sin(\bar{\varphi})}{\Delta\varphi^2\sin(\Delta\varphi)}+\frac{\cos(\bar{\varphi})}{\Delta\varphi}\right] \\
& + \frac{12R^4}{h^3}\left[-\frac{27\bar{\varphi}^2}{\Delta\varphi^3}+\frac{9\bar{\varphi}^4}{8\Delta\varphi^3}+\frac{18\bar{\varphi}}{\Delta\varphi^2}\right. \\
& - \frac{3\bar{\varphi}^3}{2\Delta\varphi^2}+\frac{\bar{\varphi}^2}{2\Delta\varphi}-\frac{45\sin(\bar{\varphi})}{2\Delta\varphi^2} \\
& + \frac{9-9\cos(\bar{\varphi})}{\Delta\varphi^2\tan(\Delta\varphi)}-\frac{1-\cos(\bar{\varphi})}{\sin(\Delta\varphi)} \\
& \left.\left. + \frac{18-18\cos(\bar{\varphi})}{\Delta\varphi^2\sin(\Delta\varphi)}\right]+\frac{R^2}{h}\left[+\frac{9\bar{\varphi}}{\Delta\varphi^2}\right.\right. \\
& \left.\left. - \frac{27\bar{\varphi}^2}{2\Delta\varphi^3}-\frac{27\sin(\bar{\varphi})}{2\Delta\varphi^2}\right]\right\},
\end{aligned}
\tag{96}
$$

$$
\begin{aligned}
\mathcal{I}_{s,1\to\varphi}(\bar{\varphi}) = & \left\{1-\nu^2\right\}\left\{\left[\frac{R^2}{h}-\frac{R}{2}-\frac{6R^3}{h^2}\right.\right. \\
& + \frac{12R^4}{h^3}\left]\left[\frac{27\bar{\varphi}\cos(\bar{\varphi})}{2(\Delta\varphi)^3}-\frac{11\bar{\varphi}\cos(\bar{\varphi})}{4\Delta\varphi}\right.\right. \\
& - \frac{27\bar{\varphi}\sin(\bar{\varphi})}{2(\Delta\varphi)^3\tan(\Delta\varphi)}+\frac{11\bar{\varphi}\sin(\bar{\varphi})}{4\Delta\varphi\tan(\Delta\varphi)} \\
& \left.\left. + \frac{27\bar{\varphi}\sin(\bar{\varphi})}{2(\Delta\varphi)^3\sin(\Delta\varphi)}-\frac{\bar{\varphi}\sin(\bar{\varphi})}{2\Delta\varphi\sin(\Delta\varphi)}\right]\right. \\
& + \left[\frac{R^2}{h}-\frac{R}{2}-\frac{6R^3}{h^2}+\frac{24R^4}{h^3}\right] \\
& \times \left[\frac{18\cos(\bar{\varphi})}{(\Delta\varphi)^2}\right]+\left[\frac{R^2}{h}-\frac{R}{2}\right]\left[\frac{27\bar{\varphi}}{(\Delta\varphi)^3}\right. \\
& - \frac{18}{(\Delta\varphi)^2}-\frac{27-27\cos(\bar{\varphi})}{4(\Delta\varphi)^3\sin(\Delta\varphi)} \\
& + \frac{1-\cos(\bar{\varphi})}{4\Delta\varphi\sin(\Delta\varphi)}-\frac{81\sin(\bar{\varphi})}{2(\Delta\varphi)^3} \\
& \left. + \frac{11\sin(\bar{\varphi})}{4\Delta\varphi}\right]+\left[\frac{12R^4}{h^3}-\frac{6R^3}{h^2}\right] \\
& \times \left[\frac{27-27\cos(\bar{\varphi})}{(\Delta\varphi)^3\tan(\Delta\varphi)}-\frac{11-11\cos(\bar{\varphi})}{2\Delta\varphi\tan(\Delta\varphi)}\right. \\
& - \frac{135-135\cos(\bar{\varphi})}{4(\Delta\varphi)^3\sin(\Delta\varphi)}+\frac{5-5\cos(\bar{\varphi})}{4\Delta\varphi\sin(\Delta\varphi)}\left.\right] \\
& + \frac{6R^3}{h^2}\left[\frac{9\bar{\varphi}^3}{4(\Delta\varphi)^3}-\frac{27\bar{\varphi}}{(\Delta\varphi)^3}+\frac{18}{2(\Delta\varphi)^2}\right. \\
& - \frac{9\bar{\varphi}^2}{2(\Delta\varphi)^2}+\frac{11\bar{\varphi}}{4\Delta\varphi}+\frac{135\sin(\bar{\varphi})}{4(\Delta\varphi)^3} \\
& \left. - \frac{33\sin(\bar{\varphi})}{8\Delta\varphi}\right]+\frac{12R^4}{h^3}\left[1-\frac{\bar{\varphi}^2}{2}\right. \\
& + \frac{81\bar{\varphi}}{(\Delta\varphi)^3}-\frac{9\bar{\varphi}^3}{(\Delta\varphi)^3}+\frac{9\bar{\varphi}^5}{40(\Delta\varphi)^3} \\
& - \frac{36}{(\Delta\varphi)^2}+\frac{18\bar{\varphi}^2}{(\Delta\varphi)^2}-\frac{3\bar{\varphi}^4}{4(\Delta\varphi)^2} \\
& - \frac{11\bar{\varphi}}{\Delta\varphi}+\frac{11\bar{\varphi}^3}{12\Delta\varphi}-\cos(\bar{\varphi}) \\
& \left.\left. - \frac{189\sin(\bar{\varphi})}{2(\Delta\varphi)^3}+\frac{55\sin(\bar{\varphi})}{4\Delta\varphi}\right]\right\},
\end{aligned}
\tag{97}
$$

$$
\begin{aligned}
\mathcal{I}_{s,4\to\varphi}(\bar{\varphi}) = & \left\{1-\nu^2\right\}\left\{\left[\frac{R^2}{h}-\frac{R}{2}-\frac{6R^3}{h^2}\right.\right. \\
& + \frac{12R^4}{h^3}\left]\left[-\frac{27\bar{\varphi}\cos(\bar{\varphi})}{2(\Delta\varphi^3)}+\frac{\bar{\varphi}\cos(\bar{\varphi})}{2\Delta\varphi}\right.\right. \\
& + \frac{27\bar{\varphi}\sin(\bar{\varphi})}{2(\Delta\varphi)^3\tan(\Delta\varphi)}-\frac{\bar{\varphi}\sin(\bar{\varphi})}{2\Delta\varphi\tan(\Delta\varphi)} \\
& \left.\left. - \frac{27\bar{\varphi}\sin(\bar{\varphi})}{2(\Delta\varphi)^3\sin(\Delta\varphi)}+\frac{11\bar{\varphi}\sin(\bar{\varphi})}{4\Delta\varphi\sin(\Delta\varphi)}\right]\right. \\
& + \left[\frac{R^2}{h}-\frac{R}{2}-\frac{6R^3}{h^2}+\frac{24R^4}{h^3}\right] \\
& \times \left[-\frac{9\cos(\bar{\varphi})}{(\Delta\varphi)^2}\right]+\left[\frac{R^2}{h}-\frac{R}{2}\right]\left[-\frac{27\bar{\varphi}}{(\Delta\varphi)^3}\right. \\
& + \frac{9}{(\Delta\varphi)^2}+\frac{27-27\cos(\bar{\varphi})}{4(\Delta\varphi)^3\sin(\Delta\varphi)}-\frac{\sin(\bar{\varphi})}{2\Delta\varphi} \\
& \left. - \frac{11-11\cos(\bar{\varphi})}{8\Delta\varphi\sin(\Delta\varphi)}+\frac{81\sin(\bar{\varphi})}{2(\Delta\varphi)^3}\right] \\
& + \left[\frac{12R^4}{h^3}-\frac{6R^3}{h^2}\right]\left[-\frac{27-27\cos(\bar{\varphi})}{(\Delta\varphi)^3\tan(\Delta\varphi)}\right. \\
& + \frac{1-\cos(\bar{\varphi})}{\Delta\varphi\tan(\Delta\varphi)}+\frac{135-135\cos(\bar{\varphi})}{4(\Delta\varphi)^3\sin(\Delta\varphi)} \\
& \left. - \frac{55-55\cos(\bar{\varphi})}{8\Delta\varphi\sin(\Delta\varphi)}\right]+\frac{6R^3}{h^2}\left[\frac{27\bar{\varphi}}{(\Delta\varphi)^3}\right. \\
& - \frac{9\bar{\varphi}^3}{4(\Delta\varphi)^3}-\frac{9}{2(\Delta\varphi)^2}+\frac{9\bar{\varphi}^2}{4(\Delta\varphi)^2} \\
& - \frac{\bar{\varphi}}{2\Delta\varphi}-\frac{135\sin(\bar{\varphi})}{4(\Delta\varphi)^3}+\frac{3\sin(\bar{\varphi})}{4\Delta\varphi}\left.\right] \\
& + \frac{12R^4}{h^3}\left[-\frac{81\bar{\varphi}}{(\Delta\varphi)^3}+\frac{9\bar{\varphi}^3}{(\Delta\varphi)^3}\right. \\
& - \frac{9\bar{\varphi}^5}{40(\Delta\varphi)^3}+\frac{18}{(\Delta\varphi)^2}-\frac{9\bar{\varphi}^2}{(\Delta\varphi)^2} \\
& + \frac{3\bar{\varphi}^4}{8(\Delta\varphi)^2}+\frac{2\bar{\varphi}}{\Delta\varphi}-\frac{\bar{\varphi}^3}{6\Delta\varphi} \\
& \left.\left. + \frac{189\sin(\bar{\varphi})}{2(\Delta\varphi)^3}-\frac{5\sin(\bar{\varphi})}{2\Delta\varphi}\right]\right\}.
\end{aligned}
\tag{98}
$$

Eqs. (60) and (63), which link the rates of the external forces to the rates of the cross section rotation angles, include the following influence functions,

$$
\mathcal{I}_{RI\to z}(\bar{\varphi}) = \left\{1-\nu^2\right\}\left\{\frac{12R^2}{h^3}\left[\frac{\cos(\bar{\varphi})-1}{\tan(\Delta\varphi)}+\sin(\bar{\varphi})-\bar{\varphi}\right]\right\},
\tag{99}
$$

$$
\mathcal{I}_{LI\to z}(\bar{\varphi}) = \left\{1-\nu^2\right\}\left\{\frac{12R^2}{h^3}\left[\frac{1-\cos(\bar{\varphi})}{\sin(\Delta\varphi)}\right]\right\},
\tag{100}
$$

$$
\begin{aligned}
\mathcal{I}_{p,1\to z}(\bar{\varphi}) = & \left\{1-\nu^2\right\}\left\{\frac{12R^3}{h^3}\left[-\bar{\varphi}-\frac{27\bar{\varphi}^2}{2(\Delta\varphi)^3}\right.\right. \\
& + \frac{9\bar{\varphi}^4}{8(\Delta\varphi)^3}+\frac{18\bar{\varphi}}{(\Delta\varphi)^2}-\frac{3\bar{\varphi}^3}{(\Delta\varphi)^2}+\frac{11\bar{\varphi}^2}{4\Delta\varphi} \\
& \left. - \frac{1-\cos(\bar{\varphi})}{\tan(\Delta\varphi)}+\sin(\bar{\varphi})-\frac{18\sin(\bar{\varphi})}{(\Delta\varphi)^2}\right. \\
& \left.\left. + \frac{18-18\cos(\bar{\varphi})}{(\Delta\varphi)^2\tan(\Delta\varphi)}+\frac{9-9\cos(\bar{\varphi})}{(\Delta\varphi)^2\sin(\Delta\varphi)}\right]\right\},
\end{aligned}
\tag{101}
$$

$$
\begin{aligned}
\mathcal{I}_{p,2\to z}(\bar{\varphi}) = & \left\{1-\nu^2\right\}\left\{\frac{12R^3}{h^3}\left[\frac{81\bar{\varphi}^2}{2(\Delta\varphi)^3}\right.\right. \\
& - \frac{27\bar{\varphi}^4}{8(\Delta\varphi)^3}\frac{45\bar{\varphi}}{(\Delta\varphi)^2}+\frac{15\bar{\varphi}^3}{2(\Delta\varphi)^2} \\
& - \frac{9\bar{\varphi}^2}{2\Delta\varphi}-\frac{45-45\cos(\bar{\varphi})}{(\Delta\varphi)^2\tan(\Delta\varphi)} \\
& \left.\left. + \frac{45\sin(\bar{\varphi})}{(\Delta\varphi)^2}-\frac{36-36\cos(\bar{\varphi})}{(\Delta\varphi)^2\sin(\Delta\varphi)}\right]\right\},
\end{aligned}
\tag{102}
$$

$$\mathcal{I}_{p,3\to z}(\bar{\varphi}) = \left\{1-\nu^2\right\}\left\{\frac{12R^3}{h^3}\left[-\frac{81\bar{\varphi}^2}{2(\Delta\varphi)^3} + \frac{27\bar{\varphi}^4}{8(\Delta\varphi)^3} + \frac{36\bar{\varphi}}{(\Delta\varphi)^2} - \frac{6\bar{\varphi}^3}{(\Delta\varphi)^2} + \frac{9\bar{\varphi}^2}{4\Delta\varphi} + \frac{36-36\cos(\bar{\varphi})}{(\Delta\varphi)^2\tan(\Delta\varphi)} - \frac{36\sin(\bar{\varphi})}{(\Delta\varphi)^2} + \frac{45-45\cos(\bar{\varphi})}{(\Delta\varphi)^2\sin(\Delta\varphi)}\right]\right\}, \tag{103}$$

$$\mathcal{I}_{p,4\to z}(\bar{\varphi}) = \left\{1-\nu^2\right\}\left\{\frac{12R^3}{h^3}\left[\frac{27\bar{\varphi}^2}{2(\Delta\varphi)^3} - \frac{9\bar{\varphi}^4}{8(\Delta\varphi)^3} - \frac{9\bar{\varphi}}{(\Delta\varphi)^2} + \frac{3\bar{\varphi}^3}{2(\Delta\varphi)^2} - \frac{\bar{\varphi}^2}{2\Delta\varphi} + \frac{9\sin(\bar{\varphi})}{(\Delta\varphi)^2} + \frac{1-\cos(\bar{\varphi})}{\sin(\Delta\varphi)} - \frac{9-9\cos(\bar{\varphi})}{(\Delta\varphi)^2\tan(\Delta\varphi)} - \frac{18-18\cos(\bar{\varphi})}{(\Delta\varphi)^2\sin(\Delta\varphi)}\right]\right\}, \tag{104}$$

$$\mathcal{I}_{s,1\to z}(\bar{\varphi}) = \left\{1-\nu^2\right\}\left\{\left[\frac{R}{h}-\frac{1}{2}-\frac{30R^2}{h^2} + \frac{60R^3}{h^3}\right]\left[\frac{27-27\cos(\bar{\varphi})}{4(\Delta\varphi)^3\sin(\Delta\varphi)} - \frac{1-\cos(\bar{\varphi})}{4\Delta\varphi\sin(\Delta\varphi)}\right] + \frac{12R^3}{h^3}\left[\frac{\bar{\varphi}^2}{2} - \frac{9\bar{\varphi}^5}{40(\Delta\varphi)^3} + \frac{3\bar{\varphi}^4}{4(\Delta\varphi)^2} - \frac{11\bar{\varphi}^3}{12\Delta\varphi}\right] + \left[\frac{12R^3}{h^3}-\frac{6R^2}{h^2}\right]\left[-\frac{27\bar{\varphi}}{(\Delta\varphi)^3} + \frac{9\bar{\varphi}^3}{2(\Delta\varphi)^3} - \frac{9\bar{\varphi}^2}{(\Delta\varphi)^2} + \frac{11\bar{\varphi}}{2\Delta\varphi} - \frac{27-27\cos(\bar{\varphi})}{(\Delta\varphi)^3\tan(\Delta\varphi)} + \frac{11-11\cos(\bar{\varphi})}{2\Delta\varphi\tan(\Delta\varphi)} + \frac{27\sin(\bar{\varphi})}{(\Delta\varphi)^3} - \frac{11\sin(\bar{\varphi})}{2\Delta\varphi}\right]\right\}, \tag{105}$$

$$\mathcal{I}_{s,4\to z}(\bar{\varphi}) = \left\{1-\nu^2\right\}\left\{\left[\frac{R}{h}-\frac{1}{2}-\frac{30R^2}{h^2} + \frac{60R^3}{h^3}\right]\left[\frac{11-11\cos(\bar{\varphi})}{8\Delta\varphi\sin(\Delta\varphi)} - \frac{27-27\cos(\bar{\varphi})}{4(\Delta\varphi)^3\sin(\Delta\varphi)}\right] + \frac{12R^3}{h^3}\left[\frac{9\bar{\varphi}^5}{40(\Delta\varphi)^3} - \frac{3\bar{\varphi}^4}{8(\Delta\varphi)^2} + \frac{\bar{\varphi}^3}{6\Delta\varphi}\right] + \left[\frac{12R^3}{h^3}-\frac{6R^2}{h^2}\right] \times \left[-\frac{\bar{\varphi}}{\Delta\varphi} + \frac{27\bar{\varphi}}{(\Delta\varphi)^3} - \frac{9\bar{\varphi}^3}{2(\Delta\varphi)^3} + \frac{9\bar{\varphi}^2}{2(\Delta\varphi)^2} + \frac{27-\cos(\bar{\varphi})}{(\Delta\varphi)^3\tan(\Delta\varphi)} - \frac{1-\cos(\bar{\varphi})}{\Delta\varphi\tan(\Delta\varphi)} - \frac{27\sin(\bar{\varphi})}{(\Delta\varphi)^3} + \frac{\sin(\bar{\varphi})}{\Delta\varphi}\right]\right\}. \tag{106}$$

Eqs. (32) and (33), i.e. the natural boundary conditions at the right and the left impost of the tunnel segment, include the following influence functions,

$$\mathcal{I}_{p,1\to RI}(\bar{\varphi}=0) = -\frac{27}{(\Delta\varphi)^3} + \frac{11}{2\Delta\varphi} - \frac{1}{\tan(\Delta\varphi)} + \frac{18}{(\Delta\varphi)^2\tan(\Delta\varphi)} + \frac{9}{(\Delta\varphi)^2\sin(\Delta\varphi)}, \tag{107}$$

$$\mathcal{I}_{p,2\to RI}(\bar{\varphi}=0) = \frac{81}{(\Delta\varphi)^3} - \frac{9}{\Delta\varphi} - \frac{45}{(\Delta\varphi)^2\tan(\Delta\varphi)} - \frac{36}{(\Delta\varphi)^2\sin(\Delta\varphi)}, \tag{108}$$

$$\mathcal{I}_{p,3\to RI}(\bar{\varphi}=0) = -\frac{81}{(\Delta\varphi)^3} + \frac{9}{2\Delta\varphi} + \frac{36}{(\Delta\varphi)^2\tan(\Delta\varphi)} + \frac{45}{(\Delta\varphi)^2\sin(\Delta\varphi)}, \tag{109}$$

$$\mathcal{I}_{p,4\to RI}(\bar{\varphi}=0) = \frac{27}{(\Delta\varphi)^3} - \frac{1}{\Delta\varphi} + \frac{1}{\sin(\Delta\varphi)} - \frac{9}{(\Delta\varphi)^2\tan(\Delta\varphi)} - \frac{18}{(\Delta\varphi)^2\sin(\Delta\varphi)}, \tag{110}$$

$$\mathcal{I}_{s,1\to RI}(\bar{\varphi}=0) = -\frac{18}{(\Delta\varphi)^2} - \frac{27}{(\Delta\varphi)^3\tan(\Delta\varphi)} + \frac{11}{2\Delta\varphi\tan(\Delta\varphi)} + \frac{27}{(\Delta\varphi)^3\sin(\Delta\varphi)} - \frac{1}{\sin(\Delta\varphi)}, \tag{111}$$

$$\mathcal{I}_{s,4\to RI}(\bar{\varphi}=0) = \frac{9}{(\Delta\varphi)^2} + \frac{27}{(\Delta\varphi)^3\tan(\Delta\varphi)} - \frac{1}{\Delta\varphi\tan(\Delta\varphi)} - \frac{27}{(\Delta\varphi)^2\sin(\Delta\varphi)} + \frac{11}{2\Delta\varphi\sin(\Delta\varphi)}, \tag{112}$$

$$\mathcal{I}_{p,1\to LI}(\bar{\varphi}=\Delta\varphi) = -\frac{27}{(\Delta\varphi)^3} + \frac{1}{\Delta\varphi} - \frac{1}{\sin(\Delta\varphi)} + \frac{9}{(\Delta\varphi)^2\tan(\Delta\varphi)} + \frac{18}{(\Delta\varphi)^2\sin(\Delta\varphi)}, \tag{113}$$

$$\mathcal{I}_{p,2\to LI}(\bar{\varphi}=\Delta\varphi) = \frac{81}{(\Delta\varphi)^3} - \frac{9}{2\Delta\varphi} - \frac{36}{(\Delta\varphi)^2\tan(\Delta\varphi)} - \frac{45}{(\Delta\varphi)^2\sin(\Delta\varphi)}, \tag{114}$$

$$\mathcal{I}_{p,3\to LI}(\bar{\varphi}=\Delta\varphi) = -\frac{81}{(\Delta\varphi)^3} + \frac{9}{\Delta\varphi} + \frac{45}{(\Delta\varphi)^2\tan(\Delta\varphi)} + \frac{36}{(\Delta\varphi)^2\sin(\Delta\varphi)}, \tag{115}$$

$$\mathcal{I}_{p,4\to LI}(\bar{\varphi}=\Delta\varphi) = \frac{27}{(\Delta\varphi)^3} - \frac{11}{2\Delta\varphi} + \frac{1}{\tan(\Delta\varphi)} - \frac{18}{(\Delta\varphi)^2\tan(\Delta\varphi)} - \frac{9}{(\Delta\varphi)^2\sin(\Delta\varphi)}, \tag{116}$$

$$\mathcal{I}_{s,1\to LI}(\bar{\varphi}=\Delta\varphi) = \frac{9}{(\Delta\varphi)^2} + \frac{27}{(\Delta\varphi)^3\tan(\Delta\varphi)} - \frac{1}{\Delta\varphi\tan(\Delta\varphi)} - \frac{27}{(\Delta\varphi)^3\sin(\Delta\varphi)} + \frac{11}{2\Delta\varphi\sin(\Delta\varphi)}, \tag{117}$$

$$\mathcal{I}_{s,4\to LI}(\bar{\varphi}=\Delta\varphi) = -\frac{18}{(\Delta\varphi)^2} - \frac{27}{(\Delta\varphi)^3\tan(\Delta\varphi)} + \frac{11}{2\Delta\varphi\tan(\Delta\varphi)} + \frac{27}{(\Delta\varphi)^3\sin(\Delta\varphi)} - \frac{1}{\Delta\varphi\sin(\Delta\varphi)}. \tag{118}$$

Finally, Eqs. (71) and (72) contain the partial derivatives of the internal force-related influence functions with respect to the opening angle $\Delta\varphi$. These derivatives read as

$$\frac{\mathrm{d}\mathcal{I}_{RI\to f}(\bar{\varphi})}{\mathrm{d}\Delta\varphi} = \frac{\sin(\bar{\varphi})}{\sin^2(\Delta\varphi)}, \tag{119}$$

$$\frac{\mathrm{d}\mathcal{I}_{LI\to f}(\bar{\varphi})}{\mathrm{d}\Delta\varphi} = -\frac{\sin(\bar{\varphi})}{\sin(\Delta\varphi)\tan(\Delta\varphi)}, \tag{120}$$

$$\frac{\mathrm{d}\mathcal{I}_{p,1\to f}(\bar{\varphi})}{\mathrm{d}\Delta\varphi} = \frac{81\bar{\varphi}}{(\Delta\varphi)^4} - \frac{27\bar{\varphi}^3}{2(\Delta\varphi)^4} - \frac{36}{(\Delta\varphi)^3} + \frac{18\bar{\varphi}^2}{(\Delta\varphi)^3} - \frac{11\bar{\varphi}}{2(\Delta\varphi)^2} + \frac{36\cos(\bar{\varphi})}{(\Delta\varphi)^3} - \frac{36\sin(\bar{\varphi})}{(\Delta\varphi)^3\tan(\Delta\varphi)} - \frac{18\sin(\bar{\varphi})}{(\Delta\varphi)^3\sin(\Delta\varphi)} - \frac{9\sin(\bar{\varphi})}{(\Delta\varphi)^2\sin(\Delta\varphi)\tan(\Delta\varphi)} + \frac{\sin(\bar{\varphi})}{\sin^2(\Delta\varphi)} - \frac{18\sin(\bar{\varphi})}{(\Delta\varphi)\sin^2(\Delta\varphi)}, \tag{121}$$

$$\frac{\mathrm{d}\mathcal{I}_{p,2\to f}(\bar{\varphi})}{\mathrm{d}\Delta\varphi} = -\frac{243\bar{\varphi}}{(\Delta\varphi)^4} + \frac{81\bar{\varphi}^3}{2(\Delta\varphi)^4} + \frac{90}{(\Delta\varphi)^3} - \frac{45\bar{\varphi}^2}{(\Delta\varphi)^3} + \frac{9\bar{\varphi}}{(\Delta\varphi)^2} - \frac{90\cos(\bar{\varphi})}{(\Delta\varphi)^3} + \frac{90\sin(\bar{\varphi})}{(\Delta\varphi)^3\tan(\Delta\varphi)} + \frac{72\sin(\bar{\varphi})}{(\Delta\varphi)^3\sin(\Delta\varphi)} + \frac{36\sin(\bar{\varphi})}{(\Delta\varphi)^2\sin(\Delta\varphi)\tan(\Delta\varphi)} + \frac{45\sin(\bar{\varphi})}{(\Delta\varphi)^2\sin^2(\Delta\varphi)}, \tag{122}$$

$$\frac{\mathrm{d}\mathcal{I}_{p,3\to f}(\bar{\varphi})}{\mathrm{d}\Delta\varphi} = \frac{243\bar{\varphi}}{(\Delta\varphi)^4} - \frac{81\bar{\varphi}^3}{2(\Delta\varphi)^4} - \frac{72}{(\Delta\varphi)^3} + \frac{36\bar{\varphi}^2}{(\Delta\varphi)^3} - \frac{9\bar{\varphi}}{2(\Delta\varphi)^2} + \frac{72\cos(\bar{\varphi})}{(\Delta\varphi)^3} - \frac{72\sin(\bar{\varphi})}{(\Delta\varphi)^3\tan(\Delta\varphi)} - \frac{90\sin(\bar{\varphi})}{(\Delta\varphi)^3\sin(\Delta\varphi)} - \frac{45\sin(\bar{\varphi})}{(\Delta\varphi)^2\sin(\Delta\varphi)\tan(\Delta\varphi)} - \frac{36\sin(\bar{\varphi})}{(\Delta\varphi)^2\sin^2(\Delta\varphi)}, \tag{123}$$

Table 2
Radial and circumferential displacement components u_r^{MPi}, u_φ^{MPi} (in meters) measured at three geodetic reflectors installed within cross section MC1452 of Sieberg tunnel; as seen in Fig. 1 of [17].

Viewing time	Measurement point MP1		Measurement point MP2		Measurement point MP3	
	u_r^{MP1}	u_φ^{MP1}	u_r^{MP2}	u_φ^{MP2}	u_r^{MP3}	u_φ^{MP3}
$t_0 = 0.000$ d	±0.00000	±0.00000	±0.00000	±0.00000	±0.00000	±0.00000
$t_1 = 0.120$ d	−0.00185	+0.00002	−0.00054	+0.00056	−0.00047	−0.00034
$t_2 = 0.252$ d	−0.00387	+0.00004	−0.00112	+0.00118	−0.00102	−0.00073
$t_3 = 0.464$ d	−0.00715	+0.00007	−0.00204	+0.00214	−0.00195	−0.00136
$t_4 = 0.792$ d	−0.01177	+0.00013	−0.00346	+0.00374	−0.00359	−0.00241
$t_5 = 1.264$ d	−0.01621	−0.00010	−0.00490	+0.00521	−0.00505	−0.00385
$t_6 = 1.750$ d	−0.01772	−0.00057	−0.00598	+0.00598	−0.00576	−0.00502
$t_7 = 2.333$ d	−0.01921	−0.00053	−0.00700	+0.00681	−0.00552	−0.00611
$t_8 = 3.500$ d	−0.02053	+0.00047	−0.00818	+0.00796	−0.00435	−0.00706
$t_9 = 4.667$ d	−0.02108	−0.00023	−0.00958	+0.00789	−0.00479	−0.00785
$t_{10} = 5.833$ d	−0.02085	−0.00065	−0.00911	+0.00832	−0.00450	−0.00956
$t_{11} = 7.000$ d	−0.02076	−0.00089	−0.00975	+0.00814	−0.00479	−0.00828
$t_{12} = 8.167$ d	−0.02062	−0.00086	−0.01026	+0.00852	−0.00430	−0.00835
$t_{13} = 9.333$ d	−0.02054	−0.00080	−0.01071	+0.00842	−0.00432	−0.00829
$t_{14} = 10.50$ d	−0.02057	−0.00077	−0.01110	+0.00843	−0.00438	−0.00818
$t_{15} = 11.67$ d	−0.02056	−0.00078	−0.01147	+0.00838	−0.00444	−0.00813
$t_{16} = 12.83$ d	−0.02054	−0.00081	−0.01192	+0.00836	−0.00449	−0.00805
$t_{17} = 14.00$ d	−0.02052	−0.00086	−0.01222	+0.00836	−0.00452	−0.00800
$t_{18} = 15.17$ d	−0.02050	−0.00092	−0.01211	+0.00814	−0.00453	−0.00802
$t_{19} = 16.33$ d	−0.02048	−0.00099	−0.01197	+0.00824	−0.00453	−0.00809
$t_{20} = 17.50$ d	−0.02047	−0.00105	−0.01178	+0.00816	−0.00450	−0.00813
$t_{21} = 18.67$ d	−0.02048	−0.00108	−0.01158	+0.00816	−0.00446	−0.00814
$t_{22} = 19.83$ d	−0.02049	−0.00107	−0.01140	+0.00811	−0.00441	−0.00813
$t_{23} = 21.00$ d	−0.02050	−0.00104	−0.01122	+0.00809	−0.00437	−0.00818

$$\frac{dI_{p,4\to f}(\bar{\varphi})}{d\Delta\varphi} = -\frac{81\bar{\varphi}}{(\Delta\varphi)^4} + \frac{27\bar{\varphi}^3}{2(\Delta\varphi)^4} + \frac{18}{(\Delta\varphi)^3} - \frac{9\bar{\varphi}^2}{(\Delta\varphi)^3} + \frac{\bar{\varphi}}{(\Delta\varphi)^2} - \frac{18\cos(\bar{\varphi})}{(\Delta\varphi)^3} + \frac{18\sin(\bar{\varphi})}{(\Delta\varphi)^3\tan(\Delta\varphi)} + \frac{36\sin(\bar{\varphi})}{(\Delta\varphi)^3\sin(\Delta\varphi)} - \frac{\sin(\Delta\varphi)}{\sin(\Delta\varphi)\tan(\Delta\varphi)} + \frac{18\sin(\bar{\varphi})}{(\Delta\varphi)^2\sin(\Delta\varphi)\tan(\Delta\varphi)} + \frac{9\sin(\bar{\varphi})}{(\Delta\varphi)^2\sin^2(\Delta\varphi)}, \tag{124}$$

$$\frac{dI_{s,1\to m}(\bar{\varphi})}{d\Delta\varphi} = \frac{27\bar{\varphi}^4}{8(\Delta\varphi)^4} - \frac{6\bar{\varphi}^3}{(\Delta\varphi)^3} + \frac{11\bar{\varphi}^2}{4(\Delta\varphi)^2} + \frac{81\sin(\bar{\varphi})}{(\Delta\varphi)^4\tan(\Delta\varphi)} - \frac{11\sin(\bar{\varphi})}{2(\Delta\varphi)^2\tan(\Delta\varphi)}, \tag{125}$$

$$\frac{dI_{s,4\to m}(\bar{\varphi})}{d\Delta\varphi} = -\frac{27\bar{\varphi}^4}{8(\Delta\varphi)^4} + \frac{3\bar{\varphi}^3}{(\Delta\varphi)^3} - \frac{\bar{\varphi}^2}{2(\Delta\varphi)^2}, \tag{126}$$

$$\frac{dI_{s,1\to f}(\bar{\varphi})}{d\Delta\varphi} = \frac{81}{(\Delta\varphi)^4} - \frac{81\bar{\varphi}^2}{2(\Delta\varphi)^4} + \frac{36\bar{\varphi}}{(\Delta\varphi)^3} - \frac{11}{2(\Delta\varphi)^2} - \frac{81\cos(\bar{\varphi})}{(\Delta\varphi)^4} + \frac{81\sin(\bar{\varphi})}{(\Delta\varphi)^4\tan(\Delta\varphi)} - \frac{11\sin(\bar{\varphi})}{2(\Delta\varphi)^2\tan(\Delta\varphi)} + \frac{11\cos(\bar{\varphi})}{2(\Delta\varphi)^2} - \frac{81\sin(\bar{\varphi})}{(\Delta\varphi)^4\sin(\Delta\varphi)} + \frac{\sin(\bar{\varphi})}{(\Delta\varphi)^2\sin(\Delta\varphi)} - \frac{27\sin(\bar{\varphi})}{(\Delta\varphi)^3\sin(\Delta\varphi)\tan(\Delta\varphi)} + \frac{\sin(\bar{\varphi})}{\Delta\varphi\sin(\Delta\varphi)\tan(\Delta\varphi)} + \frac{27\sin(\bar{\varphi})}{(\Delta\varphi)^3\sin^2(\Delta\varphi)} - \frac{11\sin(\bar{\varphi})}{2\Delta\varphi\sin^2(\Delta\varphi)}, \tag{127}$$

$$\frac{dI_{s,4\to f}(\bar{\varphi})}{d\Delta\varphi} = -\frac{81}{(\Delta\varphi)^4} + \frac{81\bar{\varphi}^2}{2(\Delta\varphi)^4} - \frac{18\bar{\varphi}}{(\Delta\varphi)^3} + \frac{1}{(\Delta\varphi)^2} + \frac{81\cos(\bar{\varphi})}{(\Delta\varphi)^4} - \frac{81\sin(\bar{\varphi})}{(\Delta\varphi)^4\tan(\Delta\varphi)} + \frac{\sin(\bar{\varphi})}{(\Delta\varphi)^2\tan(\Delta\varphi)} - \frac{\cos(\bar{\varphi})}{(\Delta\varphi)^2} + \frac{81\sin(\bar{\varphi})}{(\Delta\varphi)^4\sin(\Delta\varphi)} - \frac{11\sin(\bar{\varphi})}{2(\Delta\varphi)^2\sin(\Delta\varphi)} + \frac{27\sin(\bar{\varphi})}{(\Delta\varphi)^3\sin(\Delta\varphi)\tan(\Delta\varphi)} + \frac{11\sin(\bar{\varphi})}{2\Delta\varphi\sin(\Delta\varphi)\tan(\Delta\varphi)} - \frac{27\sin(\bar{\varphi})}{(\Delta\varphi)^3\sin^2(\Delta\varphi)} + \frac{\sin(\bar{\varphi})}{\Delta\varphi\sin^2(\Delta\varphi)}. \tag{128}$$

Data availability

All relevant data are given in the paper.

References

[1] Rabcewicz Lv. The New Austrian Tunnelling Method, part one. Water Power 1964;16:453–7.
[2] Rabcewicz Lv. The New Austrian Tunnelling Method, part two. Water Power 1964;16:511–5.
[3] Rabcewicz Lv. The New Austrian Tunnelling Method, part three. Water Power 1965;17:19–24.
[4] Karakus M, Fowell R. An insight into the New Austrian Tunnelling Method (natm). In: VII Regional Rock Mechanics Symposium (ROCKMEC'2004). Sivas, Turkey: ROCKMEC; 2004, p. 14, Conference paper, 21–22 October 2004.
[5] Sulem J, Panet M, Guenot A. An analytical solution for time-dependent displacements in a circular tunnel. Int J Rock Mech Min Sci Geomech Abstr 1987;24:155–64. http://dx.doi.org/10.1016/0148-9062(87)90523-7.
[6] Sulem J, Panet M, Guenot A. Closure analysis in deep tunnels. Int J Rock Mech Min Sci Geomech Abstr 1987;24:145–54. http://dx.doi.org/10.1016/0148-9062(87)90522-5.
[7] Fenner R. Untersuchungen zur Erkenntnis des Gebirgsdrucks (Investigations to the knowledge of the rock pressure) Glückauf, Berg- Und Hüttenmännische Z 1938;32:681–95.
[8] Pacher F. Deformationsmessungen im Versuchsstollen als Mittel zur Erforschung des Gebirgsverhaltens und zur Bemessung des Ausbaus (Measurements of deformations in experimental tunnels to explore the behavior of rock and to design the lining) Felsmech Und Ingenieurgeologie 1964;1:149–695.
[9] Jiang Y, Yoneda H, Tanabashi Y. Theoretical estimation of loosening pressure on tunnels in soft rocks. Tunn Undergr Space Technol 2001;16:99–105.
[10] Hellmich C, Macht J, Mang H. Ein hybrides Verfahren zur Bestimmung der Auslastung von Spritzbetonschalen (A hybrid method for determination of the degree of utilization of shotcrete tunnel shells) Felsbau 1999;17(5):422–5.
[11] Hellmich C, Mang H, Ulm F. Hybrid method for quantification of stress states in shotcrete tunnel shells: combination of 3D in situ displacement measurements and thermochemoplastic material law. Comput Struct 2001;79(22–25):2103–15. http://dx.doi.org/10.1016/S0045-7949(01)00057-8.
[12] Hellmich C, Pichler B, Heissenberger R, Moritz B. 150 years reliable railway tunnels–extending the hybrid method for the long-term safety assessment. Geomech Tunn 2020;13:538–46. http://dx.doi.org/10.1002/geot.202000023.
[13] Lackner R, Macht J, Hellmich C, Mang HA. Hybrid method for analysis of segmented shotcrete tunnel linings. J Geotech Geoenvironmental Eng 2002;128:298–308.
[14] Ullah S, Pichler B, Hellmich C. Modeling ground-shell contact forces in NATM tunneling based on three-dimensional displacement measurements. J Geotech Geoenvironmental Eng 2013;139:444–57.

[15] Ramspacher V, Druckfeuchter H. Baulos 3-Siebergtunnel (Construction lot 3-Sieberg tunnel) Felsbau 1999;17:84–9.
[16] Scharf R, Pichler B, Heissenberger R, Moritz B, Hellmich C. Data-driven analytical mechanics of aging viscoelastic shotcrete tunnel shells. Acta Mech 2022;233:2989–3019. http://dx.doi.org/10.1007/s00707-022-03235-1.
[17] Scharf R, Sorgner M, Scheiner S, Pichler B, Hellmich C. Viscoelasticity of hydrating shotcrete as key to realistic tunnel shell stress assessment with the new austrian tunneling method. Mech Adv Mater Struct 2024;31:13053–68. http://dx.doi.org/10.1080/15376494.2024.2332474.
[18] Scharf R. Daten-gestützte analytische Mechanik für die Neue Österreichische Tunnelbaumethode (data-driven analytical mechanics for the New Austrian Tunneling Method) [Phd thesis], TU Wien (Vienna University of Technology; 2025, http://dx.doi.org/10.34726/hss.2025.132482, [in German].
[19] Zong-Ze Y, Hong Z, Guo-Hua X. A study of deformation in the interface between soil and concrete. Comput Geotech 1995;17:75–92.
[20] Hossain MA, Yin JH. Behavior of a pressure-grouted soil-cement interface in direct shear tests. Int J Geomech 2014;14:101–9. http://dx.doi.org/10.1061/(ASCE)GM.1943-5622.0000301.
[21] Chen X, Zhang J, Xiao Y, Li J. Effect of roughness on shear behavior of red clay–concrete interface in large-scale direct shear tests. Can Geotech J 2015;52:1122–35. http://dx.doi.org/10.1139/cgj-2014-0399.
[22] Yavari N, Tang AM, Pereira JM, Hassen G. Effect of temperature on the shear strength of soils and the soil–structure interface. Can Geotech J 2016;53:1186–94. http://dx.doi.org/10.1139/cgj-2015-0355.
[23] Ilori AO, Udoh NE, Umenge JI. Determination of soil shear properties on a soil to concrete interface using a direct shear box apparatus. Int J Geo-Engineering 2017;8:2198–783. http://dx.doi.org/10.1186/s40703-017-0055-x.
[24] Haeri H, Sarfarazi V, Zhu Z, Marji MF, Masoumi A. Investigation of shear behavior of soil-concrete interface. Smart Struct Syst 2019;23:81–90. http://dx.doi.org/10.12989/sss.2019.23.1.081.
[25] Xiao S, Suleiman MT, Al-Khawaja M. Investigation of effects of temperature cycles on soil-concrete interface behavior using direct shear tests. Soils Found 2019;59:1213–27. http://dx.doi.org/10.1016/j.sandf.2019.04.009.
[26] Yazdani S, Helwany S, Olgun G. Influence of temperature on soil–pile interface shear strength. Geomech Energy Environment 2019;18:69–78. http://dx.doi.org/10.1016/j.gete.2018.08.001.
[27] Maghsoodi S, Cuisinier O, Masrouri F. Thermal effects on mechanical behaviour of soil–structure interface. Can Geotech J 2020;57:32–47. http://dx.doi.org/10.1139/cgj-2018-0583.
[28] Janipour AK, Mousivand M, Bayat M. Study of interface shear strength between sand and concrete. Arab J Geosci 2022;15:1866–7538. http://dx.doi.org/10.1007/s12517-021-09394-0.
[29] Hashemi A, Sutman M, Abuel-Naga H. Thermomechanical response of kaolin clay–concrete interface in the context of energy geostructures. Can Geotech J 2023;60:380–96. http://dx.doi.org/10.1139/cgj-2022-0172.
[30] Liu Sw, Zhang Qq, Ma B, Li Zb, Yin Wp, Lou Qg. Study on surface roughness effect on shear behavior of concrete-soil interface. Eng Fail Anal 2023;145:107050. http://dx.doi.org/10.1016/j.engfailanal.2023.107050.
[31] Li T, Zhao W, Liu R, Han J, Jia P, Cheng C. Visualized direct shear test of the interface between gravelly sand and concrete pipe. Can Geotech J 2024;61:361–74. http://dx.doi.org/10.1139/cgj-2022-0007.
[32] Podio-Guidugli P, Vianello M. Hypertractions and hyperstresses convey the same mechanical information. Contin Mech Thermodyn 2010;22:163–76. http://dx.doi.org/10.1007/s00161-010-0135-z.
[33] Stan M. Metaphysical foundations of neoclassical mechanics. In: Massimi M, Breitenbach A, editors. Kant and the laws of nature. Cambridge: Cambridge University Press; 2017, p. 214–34.
[34] Salençon J. Handbook of continuum mechanics: general concepts thermoelasticity. Springer Science & Business Media; 2001.
[35] Pham TA, Nadimi S, Sutman M. Critical review of physical-mechanical principles in geostructure-soil interface mechanics. Geotech Geol Eng 2024;42:6757–808. http://dx.doi.org/10.1007/s10706-024-02954-7.
[36] Germain P. La méthode des puissances virtuelles en mécanique des milieux continus. I: Théorie du second gradient. J de Mécanique 1973;12:235–74.
[37] Germain P. Mécanique des milieux continus. Masson, Paris: Tome I: Théorie générale; 1973.
[38] Germain P. The method of virtual power in continuum mechanics. Part 2: Microstructure. SIAM J Appl Math 1973;25(3):556–75. http://dx.doi.org/10.1137/0125053.
[39] Germain P. The method of virtual power in the mechanics of continuous media. I: Second-gradient theory. Math Mech Complex Syst 2020;8:153–90. http://dx.doi.org/10.2140/memocs.2020.8.153.
[40] Capecchi D. History of virtual work laws: a history of mechanics prospective. In: Science Networks. Historical Studies. (42):Milano, Italy: Springer Milan; 2012, p. 492, First edition.
[41] Halmos PR. Finite-dimensional vector spaces. Springer Science & Business Media; 1958.
[42] Touratier M. A refined theory of laminated shallow shells. Int J Solids Struct 1992;29:1401–15.
[43] Zhang JL, Vida C, Yuan Y, Hellmich C, Mang HA, Pichler B. A hybrid analysis method for displacement-monitored segmented circular tunnel rings. Eng Struct 2017;148:839–56. http://dx.doi.org/10.1016/j.engstruct.2017.06.049.
[44] Königsberger M, Hlobil M, Delsaute B, Staquet S, Hellmich C, Pichler B. Hydrate failure in ITZ governs concrete strength: A micro-to-macro validated engineering mechanics model. Cem Concr Res 2018;103:77–94. http://dx.doi.org/10.1016/j.cemconres.2017.10.002.
[45] Pichler B, Hellmich C. Upscaling quasi-brittle strength of cement paste and mortar: A multi-scale engineering mechanics model. Cem Concr Res 2011;41:467–76. http://dx.doi.org/10.1016/j.cemconres.2011.01.010.
[46] Pichler B, Hellmich C, Eberhardsteiner J, Wasserbauer J, Termkhajornkit P, Barbarulo R, et al. Effect of gel–space ratio and microstructure on strength of hydrating cementitious materials: An engineering micromechanics approach. Cem Concr Res 2013;45:55–68. http://dx.doi.org/10.1016/j.cemconres.2012.10.019.
[47] CEB-FIB. Model code for concrete structures 2010. Berlin, Germany: Ernst & Sohn; 2010.
[48] Scheiner S, Hellmich C. Continuum microviscoelasticity model for aging basic creep of early-age concrete. J Eng Mech 2009;135:307–23. http://dx.doi.org/10.1061/(ASCE)0733-9399(2009)135:4(307).
[49] Flores RD, Hellmich C, Pichler B. Nonlinear creep of concrete: Stress-activated stick–slip transition of viscous interfaces and microcracking-induced damage. Cem Concr Res 2025;191:107809.
[50] Irfan-ul Hassan M, Pichler B, Reihsner R, Hellmich C. Elastic and creep properties of young cement paste, as determined from hourly repeated minute-long quasi-static tests. Cem Concr Res 2016;82:36–49. http://dx.doi.org/10.1016/j.cemconres.2015.11.007.
[51] Ruiz MF, Muttoni A, Gambarova PG. Relationship between nonlinear creep and cracking of concrete under uniaxial compression. J Adv Concr Technol 2007;5:383–93. http://dx.doi.org/10.3151/jact.5.383.
[52] Tamtsia B, Beaudoin J, Marchand J. The early age short-term creep of hardening cement paste: load-induced hydration effects. Cem Concr Compos 2004;26:481–9. http://dx.doi.org/10.1016/S0958-9465(03)00079-9.
[53] Ausweger M, Binder E, Lahayne O, Reihsner R, Maier G, Peyerl M, et al. Early-age evolution of strength, stiffness, and non-aging creep of concretes: Experimental characterization and correlation analysis. Materials 2019;12(2):481–9. http://dx.doi.org/10.3390/ma12020207.
[54] Königsberger M, Irfan-ul Hassan M, Pichler B, Hellmich C. Downscaling based identification of nonaging power-law creep of cement hydrates. J Eng Mech 2016;142(12):04016106. http://dx.doi.org/10.1061/(ASCE)EM.1943-7889.0001169.
[55] Hellmich C, Ulm FJ, Mang HA. Consistent linearization in finite element analysis of coupled chemo-thermal problems with exo-or endothermal reactions. Comput Mech 1999;24:238–44.
[56] Hashin Z, et al. Analysis of composite materials. J Appl Mech 1983;50:481–505.
[57] Zaoui A. Continuum micromechanics: survey. J Eng Mech 2002;128:808–16.
[58] Fritsch A, Hellmich C. 'universal'microstructural patterns in cortical and trabecular, extracellular and extravascular bone materials: micromechanics-based prediction of anisotropic elasticity. J Theoret Biol 2007;244:597–620.
[59] Gurtin ME, Sternberg E. On the linear theory of viscoelasticity. Arch Ration Mech Anal 1962;11:291–356.
[60] Laws N, McLaughlin R. Self-consistent estimates for the viscoelastic creep compliances of composite materials. Proc R Soc A 1978;359:251–73.
[61] Benveniste Y. A new approach to the application of Mori-Tanaka's theory in composite materials. Mech Mater 1987;6:147–57.
[62] Mori T, Tanaka K. Average stress in matrix and average elastic energy of materials with misfitting inclusions. Acta Metall 1973;21:571–4.
[63] Segura NJ, Pichler BL, Hellmich C. Concentration tensors preserving elastic symmetry of multiphase composites. Mech Mater 2023;178:104555.
[64] Fritsch A, Dormieux L, Hellmich C. Porous polycrystals built up by uniformly and axisymmetrically oriented needles: homogenization of elastic properties. Comptes Rendus Mécanique 2006;334:151–7.
[65] Hershey AV. The elasticity of an isotropic aggregate of anisotropic cubic crystals. J. Appl. Mech. — Trans. ASME 1954;21(3):236–40. http://dx.doi.org/10.1115/1.4010899.
[66] Hill R. A self-consistent mechanics of composite materials. J Mech Phys Solids 1965;13:213–22.
[67] Kröner E. Berechnung der elastischen konstanten des vielkristalls aus den konstanten des einkristalls. Z. Phys. 1958;151:504–18.
[68] Ruiz M, Muttoni A, Gambarova P. Relationship between nonlinear creep and cracking of concrete under uniaxial compression. J Appl Concr Technol 2007;5(3):383–93. http://dx.doi.org/10.3151/jact.5.383.
[69] Drucker DC, Prager W. Soil mechanics and plastic analysis or limit design. Quart Appl Math 1952;10:157–65.
[70] Kupfer HB, Gerstle KH. Behavior of concrete under biaxial stresses. J Eng Mech Div 1973;99:853–66. http://dx.doi.org/10.1061/JMCEA3.0001789.
[71] Flügge W. Stresses in shells. Springer Science & Business Media; 1960.
[72] Constantinides G, Ulm FJ. The effect of two types of csh on the elasticity of cement-based materials: Results from nanoindentation and micromechanical modeling. Cem Concr Res 2004;34:67–80.
[73] Sarris E, Constantinides G. Finite element modeling of nanoindentation on c–s–h: Effect of pile-up and contact friction. Cem Concr Compos 2013;36:78–84.

[74] Scrivener KL, Crumbie AK, Laugesen P. The interfacial transition zone (itz) between cement paste and aggregate in concrete. Interface Sci 2004;12:411–21.
[75] Königsberger M, Pichler B, Hellmich C. Micromechanics of itz–aggregate interaction in concrete part i: stress concentration. J Am Ceram Soc 2014;97:535–42.
[76] Königsberger M, Pichler B, Hellmich C. Micromechanics of itz-aggregate interaction in concrete part ii: strength upscaling. J Am Ceram Soc 2014;97:543–51.
[77] Dormieux L, Molinari A, Kondo D. Micromechanical approach to the behavior of poroelastic materials. J Mech Phys Solids 2002;50:2203–31.
[78] Kreher W. Residual stresses and stored elastic energy of composites and polycrystals. J Mech Phys Solids 1990;38:115–28.
[79] Hellmich C, Ulm FJ, Mang HA. Multisurface chemoplasticity. I: Material model for shotcrete. J Eng Mech 1999;125:692–701. http://dx.doi.org/10.1061/(ASCE)0733-9399(1999)125:6(692).
[80] Ulm FJ, Coussy O. Strength growth as chemo-plastic hardening in early age concrete. J Eng Mech 1996;122:1123–32.
[81] Byfors KJ. Plain concrete at early ages. In: Technical report CBI forskning 3:80. Stockholm, Sweden: Swedish Cement and Concrete Research Institute; 1980, p. 464, Research report.
[82] Kropik C, Mang HA. Computational mechanics of the excavation of tunnels. Eng Comput 1996;13:49–69.
[83] Meschke G, Kropik C, Mang HA. Numerical analyses of tunnel linings by means of a viscoplastic material model for shotcrete. Internat J Numer Methods Engrg 1996;39:3145–62.
[84] Schreter M, Neuner M, Unteregger D, Hofstetter G. On the importance of advanced constitutive models in finite element simulations of deep tunnel advance. Tunn Undergr Space Technol 2018;80:103–13.
[85] Scharf R, Brandtner M, Moritz B, Pichler B, Hellmich C. Refined hybrid structural analysis shows plastic flexibility enhancement in NATM tunnel shell. Tunn Undergr Space Technol 2025;157:106328. http://dx.doi.org/10.1016/j.tust.2024.106328.
[86] Razgordanisharahi A, Scharf R, Pilgerstorfer T, Moritz B, Hellmich C, Pichler B. Ground-lining interaction and longitudinal joint capacity in TBM-built segmental tunnel ring: Hybrid analysis based on strain monitoring and viscoelastic shell theory. Tunn Undergr Space Technol 2026;167:106979.
[87] El Naggar H, Hinchberger SD. An analytical solution for jointed tunnel linings in elastic soil or rock. Can Geotech J 2008;45:1572–93.
[88] Son M, Cording EJ. Ground–liner interaction in rock tunneling. Tunn Undergr Space Technol 2007;22:1–9.
[89] Malmgren L, Nordlund E. Interaction of shotcrete with rock and rock bolts—a numerical study. Int J Rock Mech Min Sci 2008;45:538–53.
[90] Balduzzi G, Morganti S, Auricchio F, Reali A. Non-prismatic timoshenko-like beam model: Numerical solution via isogeometric collocation. Comput Math Appl 2017;74:1531–41.
[91] Balduzzi G, Zelaya-Lainez L, Hochreiner G, Hellmich C. Dog-bone samples may not provide direct access to the longitudinal tensile strength of clear-wood. Open Civ Eng J 2021;(15).
[92] Beuthe M. Thin elastic shells with variable thickness for lithospheric flexure of one-plate planets. Geophys J Int 2008;172:817–41.
[93] Kalousová K, Souček O, Čadek O. Deformation of an elastic shell with variable thickness: a comparison of different methods. Geophys J Int 2012;190:726–44.
[94] Brandtner M, Moritz B, Schubert P. On the challenge of evaluating stress in a shotcrete lining: Experiences gained in applying the hybrid analysis method. Felsbau 2007;25(5):93–8.
[95] Zhang JL, Hellmich C, Mang HA, Yuan Y, Pichler B. Application of transfer relations to structural analysis of arch bridges. Comput Assist Methods Eng Sci 2018;24:199–215.
[96] Benedikt J, Wagner H, Herzeg T. The St. Kanzian chain of tunnels–tunnelling under very varied and extremely difficult conditions/Tunnelkette St. Kanzian–Tunnelbau unter sehr unterschiedlichen und extrem schwierigen Bedingungen. Geomech Tunn 2016;9:405–15.
[97] Terzaghi K. Rock defects and loads on tunnel supports. In: Proctor R, White T, editors. Rock Tunnelling with Steel Supports. Youngstown, OH: Commercial Shearing Company; 1946, p. 15–99.